Computing the apparent permeability of an array of staggered square rods using volume-penalization

D.J. Lopez Penha [a,*], B.J. Geurts [a,b], S. Stolz [a,c], M. Nordlund [c]

[a] Department of Applied Mathematics, University of Twente, P.O. Box 217, 7500 AE Enschede, The Netherlands
[b] Department of Applied Physics, Eindhoven University of Technology, P.O. Box 513, 5600 MB Eindhoven, The Netherlands
[c] Philip Morris International Research & Development, Philip Morris Products SA, Quai Jeanrenaud 5, 2000 Neuchâtel, Switzerland

ABSTRACT

In the present paper we uncover through numerical simulation the velocity and pressure fields inside a model porous medium composed of an infinitely extending array of staggered square rods. These microtransport simulations allow for the prediction of macrotransport parameters that are of value to the volume-averaged description of fluid motion in porous media. We focus on computing the macroscopic apparent permeability and investigate its dependence on the Reynolds number, the porosity, and the flow direction. For the microtransport simulations a volume-penalizing immersed boundary method is presented that facilitates the computation of fluid transport in porous media, accounting for the full geometrical complexity of the porous medium. We represent porous media on uniform Cartesian grids and separate solid from fluid domains using a binary phase-indicator function. The effect of solid bodies on the fluid motion is modeled using a source term in the momentum equation. This source term approximates the no-slip condition at the solid–fluid interface.

© 2011 Elsevier Ltd. All rights reserved.

1. Introduction

Understanding transport phenomena in fibrous porous media is of key importance to many technological processes, e.g., combustion [1], particle filtration [2], and textile production [3]. Considering the wide range of length scales and complex pore geometries encountered in such media, computational predictions of transport phenomena that incorporate all geometrical complexities are very expensive. In this multiscale problem the macroscopic description is obtained using a "filtering" strategy, e.g., through volume-averaging the governing equations [4]. While filtering reduces the complexity of the problem it also creates a closure problem regarding the physical effects of sub-filter scales on the larger macroscopic scales. Our interest in this paper is the parameterization and quantification, through pore-scale simulations, of the so-called *apparent permeability* [5], i.e., a transport parameter that characterizes sub-filter scale fluid resistance. The apparent permeability takes into account both the geometrical complexity of the porous medium (i.e., pore size, shape and porosity) as well as the flow in it [5]; this in contrast to the permeability based on Darcy's law, which is a strict material property [6,7]. We will compute the apparent permeability for a porous medium composed of an infinitely extend-

ing array of staggered square rods. The effects of Reynolds number, porosity and flow direction on the apparent permeability will be investigated. The study of this model porous medium constitutes the first step toward characterizing the permeable nature of real fibrous porous media, which may be highly disordered and have arbitrarily shaped pore geometries.

To compute the apparent permeability we propose a numerical simulation strategy for solving the incompressible Navier–Stokes equations within a representative elementary volume of pore patterns. This strategy integrates a symmetry-preserving finite-volume method [8] with a 3D volume-penalizing immersed boundary method [9] to reliably simulate fluid transport in porous media. By preserving the symmetry properties of the differential operators (i.e., convective and diffusive) in the discretization allows the method to be stable on any grid resolution [8]. The incorporation of volume-penalization (also known as Brinkman penalization [10]) provides the ability to perform simulations in geometrically complex flow domains without having to construct body-conforming grids. Instead, a uniform Cartesian grid is used that spans the entire physical domain, including both the fluid and solid domains. By projecting the physical domain onto the Cartesian grid a "staircase" representation of the original (fluid and solid) domain is constructed. We then extend the equations of fluid motion into the solid parts of the physical domain and impose a vanishing velocity field by adding a forcing function to the momentum equation [9].

* Corresponding author.
E-mail address: d.j.lopezpenha@utwente.nl (D.J. Lopez Penha).

The projection of the physical domain onto a Cartesian grid will almost always result in a slight deformation of the original solid domain. Exceptions can be made for very special cases where the solid body geometry is aligned with the grid. Compared to standard body-conforming gridding strategies the solution obtained using volume-penalization will be directly affected by the grid-scale representation of the solid domains. However, this method will excel in applications where the geometry of the solid domains is not exactly known. These applications are typically concerned with geometrical data sets obtained from digital imaging techniques, e.g., computer tomography [11]. Depending on the properties of the image (e.g., noise levels and resolution) the perimeter of the solid domain is never really "sharp", it is usually only known to lie within a width of a few pixels. The projection of the digital image into a staircase representation then becomes a natural way of treating the physical domain as it closely resembles the pixel-structure of its original source. In general, the volume-penalizing immersed boundary method presented here is very well suited to address flows in very complex domains for which it is challenging to employ conventional gridding techniques to represent the domain. Particularly, at low to moderate flow complexity in the open domains, i.e., at sufficiently low Reynolds numbers, this method provides reliable predictions already at rather coarse resolutions.

Transport phenomena in porous media can be described in different forms. We distinguish between: (i) *microtransport*, in which a detailed description is given at every point in space [12] and (ii) *macrotransport*, where a spatially filtered description is adopted [13]. Each approach aims to predict the same phenomenon, but includes different physical length scales. The microtransport description offers access to all scales of transport, right down to the level of the individual pores. However, most engineering transport models are based on a macrotransport description, as this allows for a system that is computationally much less expensive. The main difficulty with the macrotransport description is the closure problem that arises from filtering the small scale flow structures. For the case of modeling fluid transport using a volume-averaged description [4], the filtered momentum equation contains a drag force which needs closing [14]. A well established closure model for the drag force [14] correlates flow effects arising at pore-scales with the averaged fluid velocity in a relation involving two transport parameters: the Darcy's law permeability tensor [6,7] and the Forchheimer tensor [14]. By incorporating both parameters into a single phenomenological dependency, quantifying the permeable nature of a porous medium, we form the *apparent permeability* [5]. Accurate macroscale flow predictions in porous media require an accurate parameterization of the apparent permeability. Performing detailed computations of the flow in a representative volume of the porous medium gives direct access to this quantity, and is the basis for the engineering closure of any macroscale transport parameter. Changes in the permeability due to changes in the local flow behavior and pore structure become evident through simulation.

Using simulation to close the drag force is a strategy widely adopted throughout literature. Many authors have studied the influence of fluid flow on the drag force for a large range of pore patterns. A large part of this research has concentrated on porous media composed of cylinders or spheres [5,15–20]. Others have considered porous media composed of rectangular shapes [21,22]. A feature common to all of these studies is the use of a body-conforming grid. This standard gridding technique is limiting when it is applied to highly complex bodies, as the design of a qualitative grid is a cumbersome task. Avoiding the use of conforming grids, the immersed boundary method is a viable alternative for simulating fluid transport in porous media. It allows for realistic geometrical complexities while maintaining an acceptable accuracy close to the solid–fluid interface. We restrict ourselves in this work to laminar flow in the pores, thereby avoiding the very high spatial resolutions that would be required to treat turbulent flow.

The proposed simulation strategy will be validated using two test cases. The first test case considers laminar, fully-developed flow between two parallel planes. Numerical results for the streamwise velocity profile will be compared with their analytical counterparts. The second test case considers flow in a model porous medium composed of an infinitely extending array of inline square rods [21,22]. A "measure" for the quality of the computed flow will be the macroscopic pressure gradient, i.e., the gradient of the intrinsically-averaged pressure. We will identify that the overall method is first-order accurate in space.

By means of a systematic numerical study, we will present results on the apparent permeability of the staggered arrangement of square rods by direct solution of the incompressible Navier–Stokes equations for a range of flow conditions. We concentrate on: A Reynolds number range $1 \leqslant \mathrm{Re} \leqslant 600$ (based on the vertical distance between two consecutive rods and the absolute value of the volume-averaged velocity); a fluid volume fraction (or porosity) of approximately 25%, 50% and 75%; and a direction of flow along each of the three coordinate axes.

Contents of this paper are organized as follows: Section 2 will discuss the closure problem encountered in the macroscopic (i.e., volume-averaged) description of fluid transport in porous media and the numerical simulation strategy used for its closure; the simulation details are discussed in Section 3 alongside reference results to validate the proposed numerical method; in Section 4 the apparent permeability is computed for the staggered arrangement of square rods as a function of the Reynolds number, the porosity, and the flow direction; and finally, a summary of the results and the conclusions is provided in Section 5.

2. Modeling fluid transport in porous media

Many problems involving fluid transport in porous media adopt a macroscopic or *filtered* description of the flow. Depending on the complexity of the flow problem several macrotransport models can be utilized. For example, for Newtonian flows at low Reynolds numbers ("creeping" flows) the well-known Darcy's law is valid. For problems involving a stronger contribution from inertial forces, a non-linear extension to Darcy's law might be more appropriate [14,23]. Much of the developments on macrotransport models for porous media have seen contributions from mainly two approaches to up-scaling the microtransport equations: the method of *volume-averaging* [4] and the method of *homogenization* [24]. In the first approach, one performs a convolution of the Navier–Stokes equations and a weighting function. A closing hypothesis is then added for the sub-filter scale source terms. The second approach uses multiscale asymptotic expansion techniques to obtain homogenized equations. As an example, the homogenized Stokes equation is Darcy's law [24].

Volume-averaging methods are widely utilized in engineering practice, especially for complex phenomena like multiphase flows with heat and mass transfer [25]. We will use volume averaging as the preferential up-scaling strategy. In this section we briefly sketch (for the purpose of completeness) the derivation of the volume-averaged Navier–Stokes equations for incompressible fluid transport in porous media (see, e.g., Ref. [14]). We will identify the macroscale transport parameters and propose a closing strategy. To handle complex porous media we will introduce the volume-penalizing immersed boundary method for simulating microtransport in arbitrary pore geometries.

2.1. Macrotransport of fluid

We consider the motion of an incompressible, Newtonian fluid in a rigid porous medium, as illustrated in Fig. 1. At the microscale, this motion is governed by the Navier–Stokes equations [12] and the accompanying boundary conditions:

$$\nabla \cdot \mathbf{u} = 0, \tag{1a}$$

$$\frac{\partial \mathbf{u}}{\partial t} + \mathbf{u} \cdot \nabla \mathbf{u} = -\frac{1}{\rho} \nabla p + \nu \nabla^2 \mathbf{u}, \tag{1b}$$

$$\mathbf{u} = 0 \quad \text{for} \quad \mathbf{x} \in A_{sf}, \tag{1c}$$

where $\mathbf{x} = (x_1, x_2, x_3)^T$ is the spatial coordinate vector and A_{sf} is the solid–fluid interface contained within the macroscopic system. The variables in the equations represent: fluid velocity $\mathbf{u} = (u_1, u_2, u_3)^T$, fluid mass-density ρ, pressure p, and kinematic viscosity $\nu \equiv \mu/\rho$; with μ the dynamic viscosity. The vector differential operator is given by the symbol $\nabla \equiv (\partial/\partial x_1, \partial/\partial x_2, \partial/\partial x_3)^T$, and the corresponding Laplace operator by $\nabla^2 \equiv \nabla \cdot \nabla$. If we assume, as sketched in Fig. 1, that the pore scale ℓ and the macroscopic scale L satisfy $\ell \ll L$, and we wish to simulate the system on the scale of L, we must resort to averaging the equations of motion to reduce the number of degrees-of-freedom in the computational model.

To derive the macroscale description of fluid motion we follow the work in Refs. [14,26]. This derivation requires the definition of two averaging operators. The first, is the *superficial volume average* (see, e.g., Refs. [27,28] for a generalized averaging procedure):

$$\langle \psi \rangle (\mathbf{x}) \equiv \frac{1}{\mathcal{V}} \int_{\mathcal{V}_f(\mathbf{x})} \psi \, dV, \tag{2}$$

where $\mathcal{V}$ is the local averaging volume (see Fig. 1), $\mathcal{V}_f$ is the fluid volume contained inside $\mathcal{V}$, and ψ is any spatial field associated with the fluid. The coordinate $\mathbf{x}$ represents the centroid of the averaging volume $\mathcal{V}$, and we assume the averaged quantity $\langle \psi \rangle$ is associated with this centroid. The size of the averaging volume must, on the one hand, be small enough such that $\langle \psi \rangle$ is characteristic of local properties around $\mathbf{x}$ and, on the other hand, be large enough to contain a representative sample of the pore topology. This size can be quantified in terms of ℓ and L for a specific porous medium. A second averaging operator is the *intrinsic volume average*, an averaging performed over the fluid volume $\mathcal{V}_f$:

$$\langle \psi \rangle^f (\mathbf{x}) \equiv \frac{1}{\mathcal{V}_f(\mathbf{x})} \int_{\mathcal{V}_f(\mathbf{x})} \psi \, dV. \tag{3}$$

Its relation with the superficial average is

$$\langle \psi \rangle = \phi \langle \psi \rangle^f, \tag{4}$$

where ϕ denotes the fluid volume fraction (or porosity):

$$\phi(\mathbf{x}) \equiv \langle 1 \rangle = \frac{\mathcal{V}_f}{\mathcal{V}}. \tag{5}$$

We can now proceed with the averaging of the equations of motion. The superficial volume average of the Navier–Stokes equations are:

$$\langle \nabla \cdot \mathbf{u} \rangle = 0, \tag{6a}$$

$$\left\langle \frac{\partial \mathbf{u}}{\partial t} \right\rangle + \langle \mathbf{u} \cdot \nabla \mathbf{u} \rangle = -\frac{1}{\rho} \langle \nabla p \rangle + \nu \langle \nabla^2 \mathbf{u} \rangle. \tag{6b}$$

Using the decomposition of ψ into its volume average $\langle \psi \rangle^f$ and fluctuation $\tilde{\psi}$ [26]:

$$\psi = \langle \psi \rangle^f + \tilde{\psi}, \tag{7}$$

our goal is to rewrite each term in Eq. (6) as a function of these variables, i.e., $\{\langle \psi \rangle^f, \tilde{\psi}\}$. We will start with the continuity equation. Using the *spatial averaging theorem* [29]:

$$\langle \nabla \psi \rangle = \nabla \langle \psi \rangle + \frac{1}{\mathcal{V}} \int_{\mathcal{A}_{sf}} \mathbf{n}_{sf} \psi \, dA, \tag{8}$$

the left hand side in Eq. (6a) is expressed as

$$\langle \nabla \cdot \mathbf{u} \rangle = \nabla \cdot \langle \mathbf{u} \rangle + \frac{1}{\mathcal{V}} \int_{\mathcal{A}_{sf}} \mathbf{n}_{sf} \cdot \mathbf{u} \, dA, \tag{9}$$

where $\mathcal{A}_{sf}$ is the solid–fluid interface contained inside $\mathcal{V}$ and $\mathbf{n}_{sf}$ is the unit surface-normal vector in the direction away from the fluid. As the velocity field vanishes on $\mathcal{A}_{sf}$ (no-slip condition), Eq. (9) reduces to
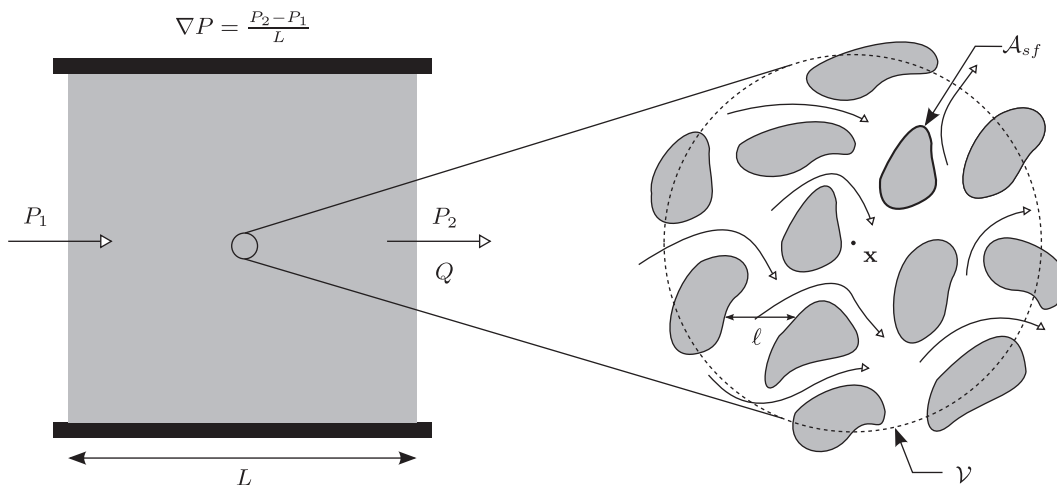
$$\langle \nabla \cdot \mathbf{u} \rangle = \nabla \cdot \langle \mathbf{u} \rangle = \nabla \cdot (\phi \langle \mathbf{u} \rangle^f) = 0, \tag{10}$$

where we made use of Eq. (4).

In the momentum equation, Eq. (6b), the average of the time derivative can be rewritten as

$$\left\langle \frac{\partial \mathbf{u}}{\partial t} \right\rangle = \frac{\partial \langle \mathbf{u} \rangle}{\partial t} = \phi \frac{\partial \langle \mathbf{u} \rangle^f}{\partial t}, \tag{11}$$

where spatial integration and time differentiation are interchangeable because $\mathcal{V}_f$ is assumed to be independent of time [see expres-

Fig. 1. Fluid transport in a rigid porous medium driven by a pressure gradient ∇P. The pressure gradient induces a flow rate Q. Left: the macroscale system of characteristic length L. Right: the spherical averaging volume $\mathcal{V}$ with its centroid located at $\mathbf{x}$, and $\mathcal{A}_{sf}$ the solid–fluid interface contained inside $\mathcal{V}$. The characteristic pore length is ℓ.

sion (2)]. Applying the spatial averaging theorem to the convective term and utilizing the no-slip boundary condition yields

$$\langle \mathbf{u} \cdot \nabla \mathbf{u} \rangle = \langle \nabla \cdot (\mathbf{u}\mathbf{u}) \rangle = \nabla \cdot \langle \mathbf{u}\mathbf{u} \rangle + \frac{1}{\mathcal{V}} \int_{\mathcal{A}_{sf}} \mathbf{n}_{sf} \cdot (\mathbf{u}\mathbf{u}) \, dA$$
$$= \nabla \cdot \langle \mathbf{u}\mathbf{u} \rangle. \tag{12}$$

By substituting Eq. (7) into the above expression and assuming a negligible variation of the averaged velocity within $\mathcal{V}$, i.e., $\langle \langle \mathbf{u} \rangle^f \rangle \approx \langle \mathbf{u} \rangle$ and $\langle \tilde{\mathbf{u}} \rangle \approx 0$ [14,26], Eq. (12) simplifies to

$$\nabla \cdot \langle \mathbf{u}\mathbf{u} \rangle \approx \phi \langle \mathbf{u} \rangle^f \nabla \cdot \langle \mathbf{u} \rangle^f + \nabla \cdot \langle \tilde{\mathbf{u}}\tilde{\mathbf{u}} \rangle. \tag{13}$$

A similar treatment can be given to the terms on the right hand side of the momentum equation. For the average of the pressure gradient [30]:

$$-\frac{1}{\rho}\langle \nabla p \rangle = -\frac{1}{\rho}\nabla(\phi \langle p \rangle^f) - \frac{1}{\mathcal{V}}\int_{\mathcal{A}_{sf}} \mathbf{n}_{sf} \frac{(\langle p \rangle^f + \tilde{p})}{\rho} \, dA$$
$$\approx -\frac{1}{\rho}\phi\nabla \langle p \rangle^f - \frac{1}{\mathcal{V}}\int_{\mathcal{A}_{sf}} \mathbf{n}_{sf} \frac{\tilde{p}}{\rho} \, dA; \tag{14}$$

where we have assumed a negligible variation of the averaged pressure within the averaging volume $\mathcal{V}$ (thereby taking it out of the surface integral), and we have made use of the relation

$$-\frac{1}{\mathcal{V}}\int_{\mathcal{A}_{sf}} \mathbf{n}_{sf} \, dA \equiv \nabla \phi, \tag{15}$$

which can easily be derived from the substitution of $\psi = 1$ into Eq. (8) and using the equality $\langle 1 \rangle = \phi$ [see expression (5)]. The average of the viscous stress term can be rewritten as [30]:

$$\nu \langle \nabla^2 \mathbf{u} \rangle = \nu \nabla^2(\phi \langle \mathbf{u} \rangle^f) + \frac{1}{\mathcal{V}}\int_{\mathcal{A}_{sf}} \mathbf{n}_{sf} \cdot \nu \nabla(\langle \mathbf{u} \rangle^f + \tilde{\mathbf{u}}) \, dA$$
$$\approx \nu \phi \nabla^2 \langle \mathbf{u} \rangle^f + \frac{1}{\mathcal{V}}\int_{\mathcal{A}_{sf}} \mathbf{n}_{sf} \cdot \nu \nabla \tilde{\mathbf{u}} \, dA + \xi; \tag{16}$$

where the term denoted by ξ is given by

$$\xi = \nu \nabla \phi \cdot \nabla \langle \mathbf{u} \rangle^f + \nu \langle \mathbf{u} \rangle^f \nabla^2 \phi, \tag{17}$$

and arises from expanding $\nabla^2(\phi \langle \mathbf{u} \rangle^f)$ and taking the term $\nabla \langle \mathbf{u} \rangle^f$ out of the surface integral. The contribution of ξ to Eq. (16) can be neglected by assuming a constant or (spatially) slowly varying porosity, for which $\xi \approx 0$. Collecting all intermediate results [Eqs. (10)–(17)] into Eq. (6) yields the intrinsically averaged Navier–Stokes equations [14]:

$$\nabla \cdot (\phi \langle \mathbf{u} \rangle^f) = 0, \tag{18a}$$

$$\frac{\partial \langle \mathbf{u} \rangle^f}{\partial t} + \langle \mathbf{u} \rangle^f \nabla \cdot \langle \mathbf{u} \rangle^f + \frac{1}{\phi}\nabla \cdot \langle \tilde{\mathbf{u}}\tilde{\mathbf{u}} \rangle$$
$$= -\frac{1}{\rho}\nabla \langle p \rangle^f + \nu \nabla^2 \langle \mathbf{u} \rangle^f + \frac{1}{\mathcal{V}_f}\int_{\mathcal{A}_{sf}} \mathbf{n}_{sf} \cdot \left(-\frac{\tilde{p}}{\rho}\mathbf{I} + \nu \nabla \tilde{\mathbf{u}} \right) dA. \tag{18b}$$

Solving the above system of equations for the variables $\{\langle \mathbf{u} \rangle^f, \langle p \rangle^f\}$ requires information from the microscale, namely information on the velocity and pressure fluctuations $\{\tilde{\mathbf{u}}, \tilde{p}\}$:

$$\frac{1}{\phi}\nabla \cdot \langle \tilde{\mathbf{u}}\tilde{\mathbf{u}} \rangle, \tag{19}$$

and

$$\frac{1}{\mathcal{V}_f}\int_{\mathcal{A}_{sf}} \mathbf{n}_{sf} \cdot \left(-\frac{\tilde{p}}{\rho}\mathbf{I} + \nu \nabla \tilde{\mathbf{u}} \right) dA. \tag{20}$$

As a consequence, we require approximate closing models for these terms expressed in averaged variables $\{\langle \mathbf{u} \rangle^f, \langle p \rangle^f\}$.

There is a close similarity between macrotransport simulations of fluid in porous media and large-eddy simulations (LES) of turbulence [31]. In LES of high-Reynolds number flows, as with macrotransport in porous media, the aim is to predict the behavior of large-scale structures in the flow; those that influence the system on a global scale [32]. The filtering strategy in LES is very much similar to volume averaging. In fact, the volume-averaging operator in its most general form [27,28] can be regarded as a generalization of the filter operator in LES. The major difference between the two operators is that in LES modeling the filter is only applied over the fluid domain, whereas in the more general volume-averaging approach both solid and fluid domains are included in the averaging volume. In the end, the volume-averaged Navier–Stokes equations [Eq. (18)] reduce to the LES equations for a domain with constant porosity $\phi = 1$, i.e., in the absence of a solid phase; where consequently no contribution is made from the integral quantity in expression (20) (cf. Ref. [33]). As with volume averaging, in LES suitable closing models must also be sought for terms containing sub-filter (or sub-grid) scale fluctuations [32].

2.2. Transport parameters and closing strategy

The averaging process of the Navier–Stokes equations has introduced two new terms that contribute to the transport of volume-averaged momentum. The first is given by the expression (19), for which $\langle \tilde{\mathbf{u}}\tilde{\mathbf{u}} \rangle$ is referred to as the sub-filter scale stress. The second is expression (20), referred to as the drag force. The sub-filter scale stress can contribute to the transport of volume-averaged momentum in a twofold process: turbulent and mechanical dispersion [33]. Here, we restrict ourselves to laminar fluid flow and ignore turbulent dispersion phenomena. Mechanical dispersion is a transport augmenting effect caused by the microscale fluid having to move around solid bodies [33]. The drag force of expression (20) is a resistance term arising from solid–fluid interaction and has its contribution attributed to a pressure and a viscous component. In Ref. [33] the authors argue that for low-Reynolds number flows the relative contribution of mechanical dispersion to the volume-averaged flow is negligible as compared to the drag force. In our description of macroscopic fluid transport we will assume that the drag force is more important than mechanical dispersion, and therefore assume a low-Reynolds number flow in the pores. To close Eq. (18), what remains is expressing the drag force in terms of the volume-averaged velocity $\langle \mathbf{u} \rangle^f$.

A closure hypothesis for the drag force has been proposed in Ref. [14], such that:

$$\frac{1}{\mathcal{V}_f}\int_{\mathcal{A}_{sf}} \mathbf{n}_{sf} \cdot \left(-\frac{\tilde{p}}{\rho}\mathbf{I} + \nu \nabla \tilde{\mathbf{u}} \right) dA = -\nu \mathbf{K}^{-1}\phi \langle \mathbf{u} \rangle^f - \nu \mathbf{K}^{-1}\mathbf{F}\phi \langle \mathbf{u} \rangle^f; \tag{21}$$

where the drag has been parameterized using the tensors $\mathbf{K}$ and $\mathbf{F}$, referred to as the permeability tensor and the Forchheimer tensor, respectively. These parameters are dependent on the type of porous medium that is being considered (i.e., the pore structure), and $\mathbf{F}$ may also be dependent on the Reynolds number of the flow in the pores.

In this work, our goal is to quantify the *permeable* nature of a porous medium using a numerical simulation strategy. Generally speaking, this means quantifying the drag force and its dependency on the Reynolds number and the direction of flow by computing its tensor parameters $\mathbf{K}$ and $\mathbf{F}$. These tensor values are ordinarily computed (cf. Ref. [22]) using the well-known Forchheimer extended Darcy's law [14]. This law can be derived from Eq. (18b) by assuming the macroscopic flow in the porous medium is stationary and uniform [and neglecting expression (19)]:

$$0 = -\frac{1}{\rho}\nabla \langle p \rangle^f - \nu \mathbf{K}^{-1}\phi \langle \mathbf{u} \rangle^f - \nu \mathbf{K}^{-1}\mathbf{F}\phi \langle \mathbf{u} \rangle^f. \tag{22}$$

Estimates for **K** and **F** are now computed using Eq. (22) and the results of microtransport simulations within a representative elementary volume (REV)[1] of the porous medium (cf. Refs. [21,22]). Our approach to quantifying the permeable nature of a porous medium closely follows the work in Ref. [5], where the concept of an *apparent permeability* was introduced. The apparent permeability tensor is a single phenomenological parameter that characterizes the drag force, and is a unification of **K** and **F**. This parameter is easier to compute as it simplifies Eq. (22). By rewriting the drag force, Eq. (22) reduces to:

$$0 = -\frac{1}{\rho}\nabla\langle p\rangle^f - \nu\mathbf{K}^{-1}(\mathbf{I}+\mathbf{F})\phi\langle\mathbf{u}\rangle^f = -\frac{1}{\rho}\nabla\langle p\rangle^f - \nu\mathbf{k}^{-1}\phi\langle\mathbf{u}\rangle^f, \quad (23)$$

where $\mathbf{k}^{-1} \equiv \mathbf{K}^{-1}(\mathbf{I}+\mathbf{F})$ is the inverse of the apparent permeability tensor; with **I** the identity tensor. Eq. (23) would be equivalent to Darcy's law [6,7] if **k** were not dependent on the Reynolds number. We will compute the apparent permeability **k** using the results of microtransport simulations within a REV. We solve the incompressible Navier–Stokes equations in the REV under the requirements of spatial periodicity and macroscopically uniform flow (i.e., **u** averaged over the REV is a constant). By averaging the microscale variables $\{\mathbf{u}, p\}$, **k** is computed through the substitution of $\{\langle\mathbf{u}\rangle^f, \langle p\rangle^f\}$ into Eq. (23).

Important to the quality of any numerical simulation strategy is the quality of its underlying spatial grid. This holds especially for simulation strategies that adopt structured body-conforming grids, as highly-skewed grid cells near strongly-curved boundaries can adversely affect the solution accuracy [34]. Porous media often have complex interconnected channels that can vary in their size and shape considerably. Producing practicable grids, whether structured or even unstructured, for such geometries is a daunting task.

To be able to deal with realistic porous media, we propose a simulation strategy that utilizes a uniform Cartesian grid. This grid will in general not be aligned with solid boundaries and the imposition of the no-slip boundary condition will proceed with the introduction of a source term in the momentum equation. This methodology is referred to as the *immersed boundary method* [9]. Specifically, we set out to solve the incompressible Navier–Stokes equations with the following modification to the momentum equations:

$$\nabla \cdot \mathbf{u} = 0, \quad (24a)$$

$$\frac{\partial \mathbf{u}}{\partial t} + \mathbf{u} \cdot \nabla\mathbf{u} = -\frac{1}{\rho}\nabla p + \nu\nabla^2\mathbf{u} + \mathbf{f}, \quad (24b)$$

where the source term **f** is given by:

$$\mathbf{f} = -\frac{1}{\epsilon}\Gamma(\mathbf{x})\mathbf{u}. \quad (25)$$

The parameter $\epsilon \ll 1$, and Γ is known as the phase-indicator function:

$$\Gamma(\mathbf{x}) \equiv \begin{cases} 0, & \text{for } \mathbf{x} \in \mathcal{V}_f \\ 1, & \text{for } \mathbf{x} \in \mathcal{V}_s \end{cases}, \quad (26)$$

with $\mathcal{V}_s$ representing the solid volume, i.e., the set difference between the REV $\mathcal{V}$ and the fluid volume $\mathcal{V}_f$ it contains. The source term acts as a "stiff spring," pushing fluid parcels that occupy the solid domain to their equilibrium positions: **u** = 0 (the no-slip condition). Further details on the methodology will follow in the next section.

3. Computing fluid transport in porous media

In the previous section we introduced the drag force in the volume-averaged Navier–Stokes equations and its unknown transport parameter the apparent permeability. We also proposed a strategy for obtaining this parameter using the microscale solution in a representative elementary volume. In this section we discuss the numerical simulation strategy for the incompressible Navier–Stokes equations in detail. The numerical method is validated against a spatially periodic model of a porous medium: an inline arrangement of square rods. We conclude with simulation results on a second spatially periodic model composed of a staggered arrangement of square rods. These basic geometries are also central to the work reported in Refs. [21,22,35].

3.1. The numerical simulation strategy

Computing the apparent permeability of a porous medium requires solving for the velocity and pressure fields in a REV, as illustrated in Fig. 2a. We denote the computational REV by $\mathcal{V}$ and solve the dimensionless form of Eq. (24) using periodic boundary conditions. The immersed boundary method with its source term **f** is used to approximate the no-slip boundary condition within $\mathcal{V}$; where $\mathcal{V}$ is the union of the fluid volume $\mathcal{V}_f$ and the solid volume $\mathcal{V}_s$.

Imposing periodicity conditions on the perimeter of $\mathcal{V}$ while retaining a non-trivial flow requires the decomposition of pressure into a periodic pressure field and a linearly varying pressure field:

$$p(\mathbf{x}, t) = \hat{p}(\mathbf{x}, t) + \nabla P \cdot \mathbf{x}, \quad (27)$$

where the symbol $(\wedge)$ denotes a spatially periodic variable. The second term on the right of Eq. (27) is required to maintain a continuous flow of fluid; with ∇P the prescribed global pressure gradient. Substituting the above pressure decomposition into the dimensionless form of Eq. (24) yields a boundary value problem for the flow variables $(\hat{\mathbf{u}}, \hat{p})$ [5]:

$$\nabla \cdot \hat{\mathbf{u}} = 0, \quad (28a)$$

$$\frac{\partial \hat{\mathbf{u}}}{\partial t} + \hat{\mathbf{u}} \cdot \nabla\hat{\mathbf{u}} = -\nabla\hat{p} + \frac{1}{\text{Re}}\nabla^2\hat{\mathbf{u}} + \mathbf{f} - \nabla P, \quad (28b)$$

where Re is the Reynolds number based on a reference velocity and length scale. We are interested in modeling macroscopically uniform flow, i.e., $\langle\hat{\mathbf{u}}\rangle = \mathbf{n}|\langle\hat{\mathbf{u}}\rangle|$ is constant in the flow direction **n**; where $|\langle\hat{\mathbf{u}}\rangle| = \sqrt{\sum_i\langle\hat{u}_i\rangle^2}$ and $i \in \{1, 2, 3\}$. We wish to maintain a constant flow rate $\mathbf{Q} = (Q_1, Q_2, Q_3)^T$ through $\mathcal{V}$ such that for $i \in \{1, 2, 3\}$:
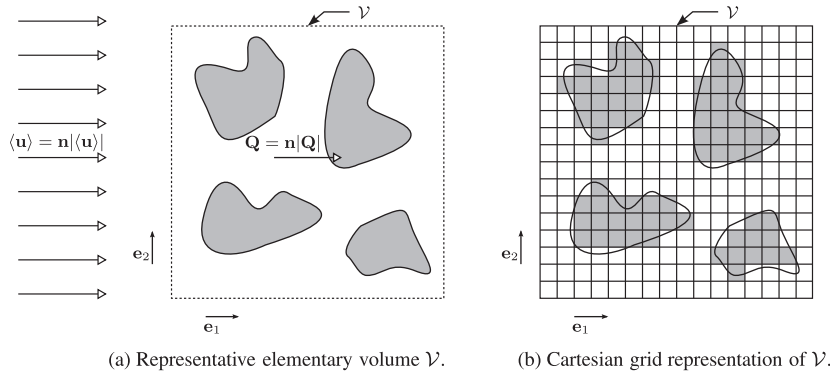
$$Q_i = \langle\hat{u}_i\rangle\mathcal{A}_i; \quad (29)$$

where $\mathcal{A}_i$ is the area of a cross-sectional plane of $\mathcal{V}$ with its normal in the direction of the coordinate axis x_i. As a general consequence, the global pressure gradient ∇P is time and Reynolds number dependent. Under a predefined and constant $\mathbf{Q} = \mathbf{n}|\mathbf{Q}|$, we adapt the global pressure gradient ∇P necessary to maintain this rate of flow at each instant in time in our algorithm. The computed global pressure gradient will function as a correction to the periodic pressure field $\hat{p}$. We illustrate the algorithm using a fractional step method [36] and a simple Euler-forward integrator for the temporal derivative. In a single time-step we distinguish a number of key operations:

1. Solve for the intermediate velocity $\hat{\mathbf{u}}^*$:

$$\frac{\hat{\mathbf{u}}^* - \hat{\mathbf{u}}^n}{\Delta t} = \left[-\hat{\mathbf{u}} \cdot \nabla\hat{\mathbf{u}} + \frac{1}{\text{Re}}\nabla^2\hat{\mathbf{u}}\right]^n + \mathbf{f}^*, \quad (30a)$$

where Δt is the time-step and the superscript n denotes the value at time $t = n\Delta t$. We treat the source term **f** of the immersed boundary method implicitly as to avoid severe stability constraints on Δt.

---

[1] A representative elementary volume [7] is the smallest unit of volume that, when repeated periodically, approximates the porous medium. For disordered porous media, a proper representative elementary volume must characterize the important statistics of the flow.

(a) Representative elementary volume $\mathcal{V}$.   (b) Cartesian grid representation of $\mathcal{V}$.

Fig. 2. Macroscopically uniform flow in a porous medium with a representative elementary volume $\mathcal{V}$. The uniform flow field induces a constant flow rate $\mathbf{Q}$ of strength $|\mathbf{Q}|$ and direction $\mathbf{n}$ in $\mathcal{V}$ (a). Solid bodies are approximated in $\mathcal{V}$ using a Cartesian grid representation, where grid cells function as units of "matter" (solid or fluid) (b).

2. Solve for $\hat{p}$ in the pressure-Poisson equation:

$$\nabla^2 \hat{p} = \frac{1}{\Delta t} \nabla \cdot \hat{\mathbf{u}}^*. \tag{30b}$$

3. Update the velocity to satisfy the divergence-free constraint:

$$\hat{\mathbf{u}}^{**} = \hat{\mathbf{u}}^* - \Delta t \nabla \hat{p}. \tag{30c}$$

4. Compute the instantaneous flow rate for $i \in \{1, 2, 3\}$ (without pressure correction):

$$Q_i^{**} = \int_{\mathcal{A}_i} \mathbf{e}_i \cdot \hat{\mathbf{u}}^{**} \, dA, \tag{30d}$$

with $\mathbf{e}_i$ the unit vector along the x_i-axis. The pressure correction ∇P is derived from the difference between the specified flow rate and the instantaneous flow rate:

$$Q_i - Q_i^{**} \equiv \Delta Q_i = \int_{\mathcal{A}_i} \mathbf{e}_i \cdot \Delta t \nabla P \, dA, \tag{30e}$$

where $Q_i = \mathbf{e}_i \cdot \mathbf{n} |\mathbf{Q}|$. Solving for the instantaneous ∇P, gives:

$$\mathbf{e}_i \cdot \nabla P = \frac{\Delta Q_i}{\Delta t \mathcal{A}_i}. \tag{30f}$$

5. Finally, compute the field variables $\hat{\mathbf{u}}^{n+1}$ and p^{n+1} at the next time-step:

$$p^{n+1} = \hat{p} + \nabla P \cdot \mathbf{x}, \tag{30g}$$
$$\hat{\mathbf{u}}^{n+1} = \hat{\mathbf{u}}^* - \Delta t \nabla p^{n+1}. \tag{30h}$$

The superscript $n + 1$ denotes the value at $t = (n + 1)\Delta t$ and the velocity field $\hat{\mathbf{u}}^{n+1}$ satisfies the divergence-free constraint.

We solve for the flow variables $\{\hat{\mathbf{u}}, p\}$ in Eq. (30) using a symmetry-preserving finite-volume method on a staggered grid [8]. This method preserves the symmetry properties of the differential operators (i.e., convective and diffusive) such that it is stable on any grid resolution and conserves the total mass, momentum and energy (the latter only for inviscid flows). We integrate in time using an explicit time-stepping algorithm of Adams–Bashforth type [8]. Formally, the discretized system is both second-order accurate in space and time. However, the treatment of the no-slip boundary condition using the immersed boundary method reduces the spatial order of convergence to first-order. This will be demonstrated in Section 3.2 using the simple test case of laminar plane channel flow.

Having a first-order accurate method implies slow convergence to the solution, and generally high spatial resolutions are required to obtain quantitatively accurate results. As a consequence, the computational requirements are relatively high. In the applications considered in Sections 3.3 and 4 a typical problem of $\sim 2.6 \times 10^5$

degrees-of-freedom at a Reynolds number of Re = 1 is solved on 1 processor of an IBM Power6 machine in ~ 6 h. For higher Reynolds numbers the simulation time increases further, e.g., at Re = 100 the simulation time increases to ~ 110 h to reach full steady state (up to eight decimal places). Improvements on the algorithm's design and an extension to parallel processing is being implemented.

The choice of time-step Δt is of importance for both the accuracy and the stability of the time integration method. Our interest in this work lies mainly with steady flow problems and we are therefore primarily concerned with a choice of Δt based on numerical stability. For example, if the Reynolds number of the flow and/ or the spatial resolution change, the choice of Δt will be adapted accordingly to maintain stability of the explicit scheme. We also opt for a fixed time-step per simulation and ignore any adaptive time-stepping strategies. Contrary to a fully explicit scheme, it is also commonly practiced in turbulent flow simulations of incompressible fluids to treat the viscous term implicitly in the time integration [37]; thus benefiting from a less restrictive time-step and therefore possibly reducing the computational work. Such a gain in computational efficiency might also be possible for low-Reynolds number simulations of steady flows. We have, however, not considered such an approach as our integration strategy has a favorable extended range of stability [8] and is very suitable for our applications.

In the following subsection we discuss in more detail the immersed boundary method. We will focus on a specific type of immersed boundary method: *volume penalization*.

3.2. The immersed boundary method: volume penalization

The *immersed boundary (IB) method* gets its name from its characteristic feature that solid bodies are "immersed" in a Cartesian grid that, generally, does not conform to their boundaries [9]. In other words, the computational grid is constructed without much regard for the solid bodies. On this nonbody-conforming grid the effect of an immersed body on the flow of fluid, ordinarily represented by boundary conditions, is reproduced using a source term (or forcing function) in the momentum equation. This forcing function is to simulate the net momentum exchange between the fluid and solid, thereby approximating the no-slip condition at their interface.

The advantage of the IB method is the relative ease with which it can approximate flows in and around geometrically complex bodies. This is most evident in the pioneering work of Ref. [38], where the IB method was first developed to simulate cardiac mechanics and associated blood flow. The author was able to replace the use of a moving, body-conforming grid with a static

Cartesian grid; avoiding complex regridding strategies for the heart. Even for simulations requiring static grids of complex domains, the generation of a body-conforming grid of practicable quality is a time-consuming process. The resulting grids are generally prone to various abnormalities, such as: highly-skewed grid cells or cells with large aspect ratios; all of which can negatively influence the solution accuracy and convergence rate of the solver. These abnormalities are clearly not present in Cartesian grids.

In general, IB methods require more computational nodes than their body-conforming counterparts. However, they can compensate by taking advantage of efficient and fast numerical methods [9]. The major difficulty with the IB method remains the imposition of boundary conditions, and therefore the definition of a proper forcing function. The treatment of the boundary conditions will have an obvious effect on the local and global behavior of the system. Despite this difficulty, the IB method has steadily gained acceptance as a very capable method for simulating flows around geometrically complex bodies.

Various forcing strategies have been developed for the IB method. Most of the popular strategies operate in the discrete regime, that is, their definitions arise after the governing equations have been discretized (refer to Ref. [9] and the many references therein). Primary advantages of this type of treatment are the robustness of the forcing functions (no added stability constraints) and the ability to sharply represent boundaries; thereby enabling higher ranges of the Reynolds number. On the other hand, these treatments are much more difficult to implement (e.g., the cut-cell method) and they require a detailed knowledge of the physical interface, such as: surface normals and curvature. Also, in some practical applications, the availability of interface data might only be limited to imaging techniques (e.g., computer tomography), where the amount of spatial (pixel) resolution can limit proper interface reconstruction.

In this work we consider a continuous forcing function of the "volume penalizing" type [39,40]. It is continuous because its definition is of physical basis, and is directly incorporated into the continuous formulation of the equations. It is volume-penalizing because the forcing extends throughout the entire solid body and is not just confined to a neighborhood of the physical interface. What makes volume-penalization an attractive method is not only its ease of implementation, but also its use of a *phase-indicator function*. This method uses the phase-indicator function to identify regions of space occupied by the solid body, and then "forces" the no-slip boundary condition through penalizing a measured difference between the actual and desired solid volume velocity. Mathematically, we have a very simple expression for the forcing function:

$$\mathbf{f} = -\frac{1}{\epsilon} \Gamma(\mathbf{x})(\mathbf{u} - \mathbf{u}_s), \tag{31}$$

where $\mathbf{u}_s$ is a prescribed solid (rigid) body velocity and Γ is the binary phase-indicator function:

$$\Gamma(\mathbf{x}) = \begin{cases} 0, & \mathbf{x} \in \mathcal{V}_f \\ 1, & \mathbf{x} \in \mathcal{V}_s \end{cases}. \tag{32}$$

The positive parameter $\epsilon \ll 1$ controls the effectiveness of the forcing function. By decreasing ϵ, the magnitude of $\mathbf{f}$ (in the solid and at the solid–fluid interface) will grow beyond the level of the remaining flux terms in the momentum equation, effectively reducing the momentum equation to the simple form: $\partial \mathbf{u}/\partial t = \mathbf{f}$. This equation will, at an exponential rate, force the velocity difference $\mathbf{u} - \mathbf{u}_s$ to a negligibly small value [41]. The function Γ allows the forcing to be active only within the solid domain. Within the fluid domain, the forcing vanishes completely and the governing equations of motion are the standard incompressible Navier–

Stokes equations. To avoid stability problems with the forcing function, its contribution to the total flux is treated implicitly in the time-advancing scheme [see Eq. (30a)].

In the discrete space, the phase-indicator function Γ is approximated by a discrete equivalent Γ_h on a uniform Cartesian grid. But, as solid bodies are seldom aligned with this grid, imposing boundary conditions on the "true" boundary location is difficult. The volume-penalization method circumvents this difficulty by allowing a "less refined" definition of the solid geometry: A *Cartesian grid representation*. By choosing a single Cartesian grid cell as the smallest unit of physical space, a solid body is then approximated by a collection of these cells; leading to a "staircase" approximation of the solid and fluid domains, as illustrated in Fig. 2b. In this way we distinguish between grid cells that are either completely solid or completely fluid. Contrary to volume-of-fluid methods [42], grid cells cannot be partially filled by solid. The Cartesian grid representation greatly simplifies the definition of Γ_h and the algorithmic implementation of the forcing function $\mathbf{f}$. In fact, the staircase or "pixelated" geometries are very similar to the way a digital image is represented on a computer. Each image is comprised of a series of pixels of a certain color and a fixed width (or grid resolution); these are all properties shared by the phase-indicator function with its "binary color palette". By increasing the grid resolution of the image we improve its clarity and sharpness, this also holds true for the Cartesian grid representation of a solid body. As a direct consequence of this analogy, the volume-penalizing IB method is well suited to approximate flows in domains extracted through computer imaging techniques.

The method of volume-penalization originated from the work of Arquis and Caltagirone [39], where they studied natural convection in a fluid-porous cavity. The reasoning behind their forcing strategy is borrowed from the field of flow in porous media, where the added resistance experienced by the fluid is approximated by the *Darcy drag*: $\mathbf{f} = -(\nu/K)\mathbf{u}$. Here $K(\mathbf{x})$ is the space dependent permeability, for which $K = \infty$ in the fluid domain and $K = 0$ in the solid domain. If we assume $\nu K^{-1}(\mathbf{x}) = \epsilon^{-1}\Gamma(\mathbf{x})$, we return to the original formulation in expression (31) (for $\mathbf{u}_s = 0$). A highly impermeable porous medium is approximated by taking $\epsilon \to 0$ (and thereby $K \to 0$), where the velocity $\mathbf{u}$ reduces to a negligibly small value.

We conclude this subsection by demonstrating the order of accuracy of the volume-penalizing IB method for laminar, fully-developed flow between two parallel planes. This flow is a simple yet powerful test case, as the quality of the developed velocity profile, a parabola, is completely determined by the accuracy with which the wall-friction (or velocity gradient) is approximated at the boundaries.

3.2.1. Laminar plane channel flow

Laminar plane channel flow, also known as plane-Poiseuille flow, is a well documented problem (see, e.g., Ref. [43]), one for which the analytical velocity profile is a known function of the applied global pressure gradient [43]. In the numerical simulation we will approximate the channel walls by penalizing grid cells in the wall domain, thereby creating "fictitious walls" that are two grid cells thick (see Fig. 3). The implicit treatment of the forcing function [see expression (31)] allows for very small values for the effectivity parameter. Numerical experimentation has shown negligible dependence of the solution on ϵ for values below 10^{-8}. Here, we adopt $\epsilon = 10^{-10}$, for which the solid–fluid interface is well localized to within one grid cell.
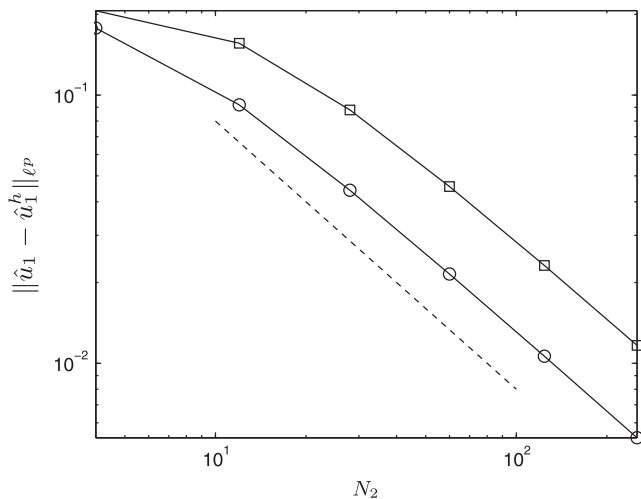
By computing the streamwise velocity component (assuming the direction of flow is along the x_1-axis; x_2 is the wall-normal axis) the error relative to the analytical velocity profile can be obtained. Theory prescribes, and the numerical results have confirmed, that the solution profile is independent of the directions $\{x_1, x_3\}$ [43]. Errors are therefore computed only along the x_2-axis. The norm
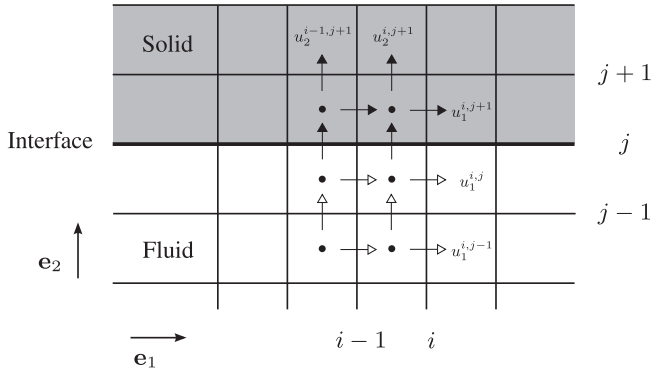
Fig. 3. Close up of a near interface region for flow between two parallel planes. The solid–fluid interface is located on a grid line. The grid is of staggered arrangement, where the velocity components $\{u_1, u_2, u_3\}$ are located on the faces of the control volumes. Filled arrow heads are used to represent components of the velocity that are penalized using the immersed boundary method. Empty arrow heads represent those components that are exempt from penalization, and are governed by the standard incompressible Navier–Stokes equations.

of the error as a function of the wall-normal grid resolution is illustrated in Fig. 4. The grid resolution is taken from the set $N_2 \in \{2^m | m = 3, \ldots, 8\}$. The ℓ^2-norm represents the square vector-norm: $\sqrt{1/N_2 \sum (\hat{u}_1 - \hat{u}_1^h)^2}$, with summation performed over all computational nodes. With the ℓ^∞-norm we indicate the maximum-norm, or the maximal computed deviation from the analytical solution: $\max |\hat{u}_1 - \hat{u}_1^h|$, with the maximum determined over all computational nodes. From Fig. 4 we can conclude that the velocity field converges at a rate that is consistent with a first-order method. This behavior is attributed to the fact that the solid–fluid interface is not aligned with all the three velocity components (see Fig. 3). As a consequence, the no-slip condition is not *fully* satisfied at this location. The real interface is actually localized to within half a grid cell. It is this slight, but unavoidable "non-alignment" of the interface with the underlying staggered grid arrangement that produces the observed decay rate of error in velocity.

More general flow domains that cannot be aligned with the grid introduce a second component to the error. The error in the computed velocity field is not only affected by the error in the spatial discretization but also by the error in the non-alignment of the

Fig. 4. ℓ^p-norm of error in velocity $\|\hat{u}_1 - \hat{u}_1^h\|_{\ell^p}$ as a function of the wall-normal grid resolution N_2 for flow between two parallel planes; with $p \in \{2, \infty\}$. The computed streamwise velocity component is given by $\hat{u}_1^h$. The ℓ^2-norm of the error is indicated by the ($\bigcirc$)-markers and the ℓ^∞-norm by the ($\square$)-markers. The dashed line represents a negative slope of one.

geometry with the grid. For laminar flow inside a tube of circular cross section we have confirmed that the velocity field also converges linearly [44]. Capturing of the separation region associated with flow *over* a cylinder is more challenging since the line of separation is not localized at the sharp edges of the interface as in the current Cartesian grid representation. The matter of geometrical convergence and the quality of the accompanying flow field will be the topic of future works.

3.3. Model porous media: flow in spatially periodic arrays of square rods

In this subsection we compute microscale velocity and pressure fields for two spatially periodic models of a porous medium, as illustrated in Fig. 5. Both models are composed of infinitely extending square rods; which allows for the solid bodies to be aligned with the underlying Cartesian grid. The solution of the first model, an inline arrangement, is compared with reference values from literature. The second model is a staggered arrangement, and its microscale solutions are post-processed in Section 4 to obtain the apparent permeability. For simplicity of notation we will drop all ($\wedge$)-symbols in future references to spatially periodic velocity fields.
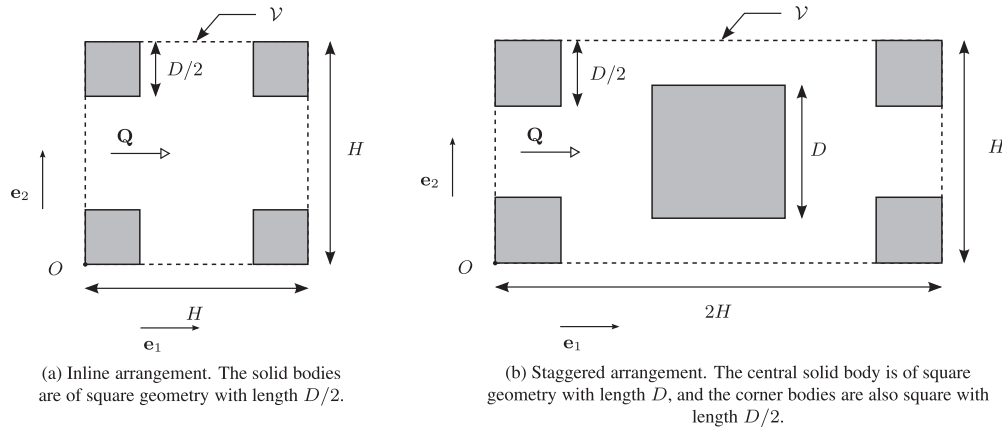
3.3.1. Inline arrangement

Consider macroscopically uniform flow in a porous medium with a REV as illustrated in Fig. 5a. The solid body in each corner is assumed square and of length $D/2$ (as $\mathcal{V}$ is periodic, outside $\mathcal{V}$ the solid body is square and of length D; cf. Refs. [21,22]). We take $\mathcal{V}$ to be of area $H \times H$, and maintain a fixed porosity $\phi = 1 - (D/H)^2 = 0.75$. Depth is created in $\mathcal{V}$ by extruding the solid content along the x_3-axis over a length H; thereby modeling infinitely extending rods. The direction of flow is along the x_1-axis (i.e., $\mathbf{n} = \mathbf{e}_1$) and numerical simulations at various Reynolds numbers will be compared with those in Refs. [21,22]. The grid resolution will also be varied in order to investigate the convergence properties of the proposed IB method. A "measure" for the simulated flow will be the *macroscopic pressure gradient* [21,22]: $\partial \langle p \rangle^f / \partial x_1$ (i.e., the gradient of the intrinsic-averaged pressure along the x_1-axis). This pressure gradient is equivalent to the global pressure gradient $\mathbf{e}_1 \cdot \nabla P$ in Eq. (30f).

We assume H and the absolute value of the macroscopic velocity $|\langle \mathbf{u} \rangle|$ as our reference scales, thereby obtaining the Reynolds number $Re = H|\langle \mathbf{u} \rangle|/\nu$. The range of Reynolds numbers is taken from the set $Re \in \{1 \times 10^m, 2 \times 10^m, 6 \times 10^m | m = -1, 0, 1, 2\}$. By requiring a constant dimensionless macroscopic velocity of $|\langle \mathbf{u} \rangle| = \langle u_1 \rangle = 1$, we set the flow rate $\mathbf{Q} = (1, 0, 0)^T$. For the porosity $\phi = 0.75$, the solidity or solid volume fraction $[1 - \phi = (D/H)^2]$ is 25% of the total volume of $\mathcal{V}$. Therefore, 25% of the grid cells are dedicated to the solid domain and 75% of the cell to the fluid domain. To achieve the desired porosity under a constant H, the length D must satisfy: $D = \sqrt{1 - \phi} H$. As a solid body is represented by a collection of grid cells, the length D can also be expressed in terms of the number of grid cells N_D across D, i.e., $D = N_D \Delta x_2$. Here, $N_D = \sqrt{1 - \phi} N_2$, N_2 is the grid resolution along the x_2-axis, and Δx_2 is the grid spacing along the x_2-axis. We require the condition that $N_D/2$ is an integer value in order to correctly represent the solid bodies on the underlying grid. As an example, a grid resolution in the (x_1, x_2)-plane of $N_1 \times N_2 = 64 \times 64$, spans $N_D = 32$ grid cells across D ($\phi = 0.75$); and resulting in 32 grid cells across the "inlet" at $x_1 = 0$ [see Fig. 5a].

Results for the velocity vector field are presented in Fig. 6 for two values of the Reynolds number $Re \in \{1, 100\}$. The grid resolution is $N_1 \times N_2 = 64 \times 64$. Along the x_3-axis we maintain a constant minimal resolution of $N_3 = 4$, as the solid bodies are assumed of infinite length. At $Re = 1$, the flow field slightly deviates from its

(a) Inline arrangement. The solid bodies are of square geometry with length $D/2$.

(b) Staggered arrangement. The central solid body is of square geometry with length D, and the corner bodies are also square with length $D/2$.

Fig. 5. Representative elementary volume $\mathcal{V}$ (with origin O) for two spatially periodic models of a porous medium. The solid bodies in the (x_1, x_2)-plane are extruded along the x_3-axis over a depth H to form a three-dimensional elementary volume. A fixed flow rate $\mathbf{Q} = \mathbf{n}|\mathbf{Q}|$ is imposed in the direction $\mathbf{n}$. Both models include solid bodies that can be aligned with the underlying Cartesian grid.

bulk motion and flows into, and out of, the upper and lower cavities. By increasing the Reynolds number, two counter-rotating vortices or recirculation zones develop, causing the bulk flow to resemble laminar (Poiseuille) flow between two parallel planes. At Re = 100, these vortices remain steady in time. It is also evident that the IB method has forced the computational nodes within the solid bodies to have a vanishing velocity.

In Table 1, simulation results for the macroscopic pressure gradient are compared with results obtained in Ref. [21] using a non-uniform, body-conforming grid of resolution $N_1 \times N_2 = 181 \times 181$. Results are compared at three Reynolds numbers and at three grid resolutions. We characterize differences in the two data sets using the percentage error $\delta(\psi)$, i.e., the relative error times 100%:

$$\delta(\psi) \equiv \frac{\psi_h - \psi}{\psi} \times 100\%, \tag{33}$$

where ψ is the true solution and ψ_h its approximation. It is evident that doubling the grid resolution in both the x_1 and x_2 directions reduces the percentage error by about half (≈ 0.55). This again demonstrates that the method is first-order accurate in space. It is also evident from the Re = 600 simulations that the percentage errors are slightly higher as compared to the previous two Reynolds numbers. This difference can be attributed to the increased velocity gradients near boundaries; these become increasingly difficult to approximate using uniform grid spacings.

In Fig. 7 the macroscopic pressure gradient is plotted for the range of Reynolds numbers Re $\in \{1 \times 10^m, 2 \times 10^m, 6 \times 10^m | m = -1, 0, 1, 2\}$ (still remaining within the laminar flow regime) and at a grid resolution of $N_1 \times N_2 = 64 \times 64$. The solid line is a model relation for the macroscopic pressure gradient [21,22]. It is the Forchheimer extended Darcy's law:

$$-\frac{\partial \langle p \rangle^f}{\partial x_1} \approx a \, \mathrm{Re}^{-1} + c, \tag{34}$$

where the parameters $\{a, c\}$ are approximated through numerical simulation: $a = 76$ and $c = 0.2$ [21,22]. This model extends the applicability of the linear Darcy's law [30] to compensate for stronger inertial effects at higher Reynolds numbers. Also plotted in Fig. 7 with ($\times$)-markers are values for the macroscopic pressure gradient at Re $\in \{10, 100, 600\}$, as found in Ref. [21]. Good agreement is seen between the numerical results and the proposed model in its linear regime (Re $\leqslant 20$). However, for larger Reynolds numbers, expression (34) overpredicts the pressure gradient and prematurely starts to level out.

The results presented in Table 1 and Fig. 7 have made it clear that the volume-penalizing IB method can be a reliable tool for predicting fluid transport. Although a high resolution is required to obtain converged results, reliable trends are already visible at very moderate resolutions. The strength of the method, however, remains its "gridding free" strategy, that is, the ability to produce qualitative results on a Cartesian grid without the added hassle of designing practicable grids.

3.3.2. Staggered arrangement

The staggered arrangement of square rods [see Fig. 5b], first presented in Ref. [35] for convective heat transfer computations, is of interest when considering models of porous media representing anisotropic "bundles" of solid material. Although the arrangement is structured, it remains a good basic model for approaching unstructured, rectangularly shaped, slender geometries. Similar to the previous case, we will compute the local velocity and pressure fields within this staggered arrangement and analyze the resulting flow patterns.

Once again, consider macroscopically uniform flow in a porous medium with a REV as illustrated in Fig. 5b: $\mathcal{V} = 2H \times H \times H$. Depth in $\mathcal{V}$ is created by extruding the solid content along the x_3-axis over a length H. All solid bodies are of square shape, where the central body has a length D and the four corner bodies lengths $D/2$. The porosity is given by $\phi = 1 - (D/H)^2 = 0.75$, thereby $D = H/2$. We will perform flow simulations along the $\{x_1, x_2\}$-axes (i.e., $\mathbf{n} \in \{\mathbf{e}_1, \mathbf{e}_2\}$) for two values of the Reynolds number Re $\in \{1, 100\}$ (we maintain similar reference scales for the velocity and length as for the inline geometry). Of interest are the differences in flow-structures observed during the transition from a predominantly viscous regime to a more inertial regime, i.e., Re = 1 to Re = 100. These (local) differences will contribute to a change in the drag force experienced by the fluid. This will also have definite consequences for the macroscopic flow properties, as will become evident when we consider the apparent permeability in Section 4.

Under the constant macroscopic flows $|\langle \mathbf{u} \rangle| = \langle u_1 \rangle = 1$ (i.e., $Q_1 = 1$) and $|\langle \mathbf{u} \rangle| = \langle u_2 \rangle = 1$ (i.e., $Q_2 = 2$), we plot their respective velocity vector fields for Re $\in \{1, 100\}$ in Fig. 8. The grid resolution in the (x_1, x_2)-plane is $N_1 \times N_2 = 128 \times 64$. It is immediately apparent from a comparison between the two orthogonal flow directions that the flow along the x_1-axis experiences a larger deviation from its bulk motion than the flow along the x_2-axis. The fluid in Fig. 8a and b is forced to move around the center body, while in Fig. 8c and d it moves mainly between the solid bodies. This difference will result in a larger drag force (at equal Reynolds number) along the x_1-axis.

(a) Re = 1.

(b) Re = 100.
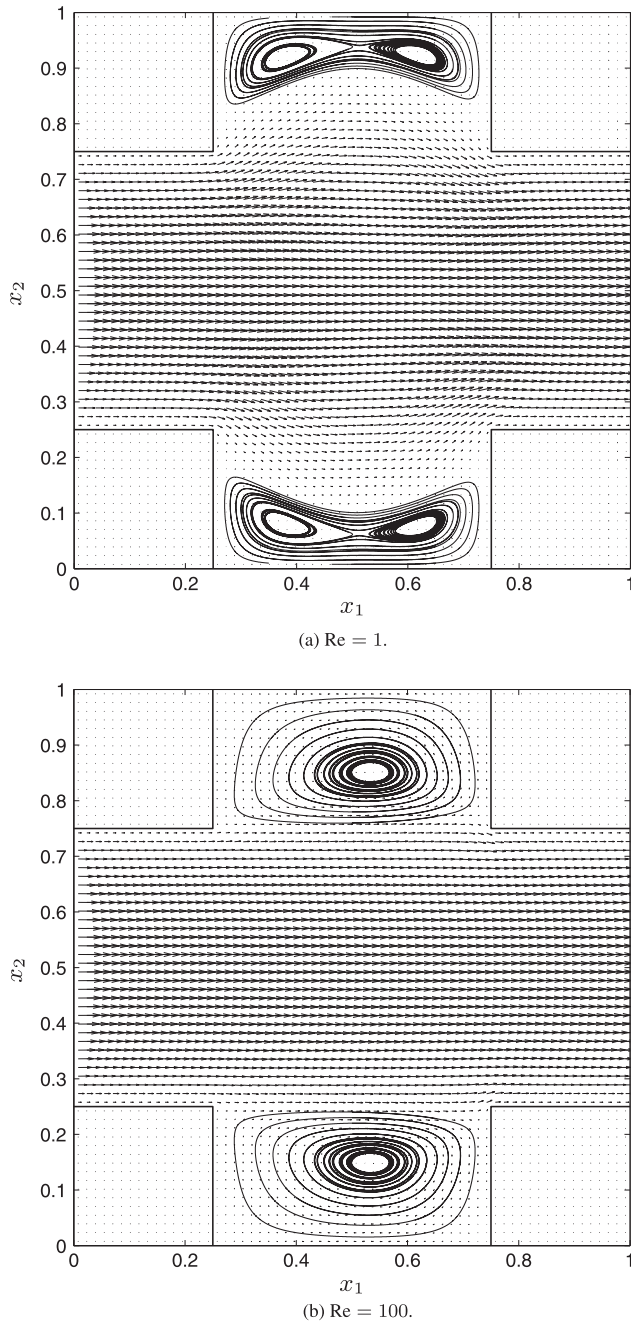
Fig. 6. Velocity vector field in the (x_1, x_2)-plane at two values of the Reynolds number Re $\in \{1, 100\}$ for the inline arrangement of square rods. The streamlines help visualize the dynamics in the upper and lower cavities. The porosity $\phi = 0.75$ and the grid resolution in the (x_1, x_2)-plane is $N_1 \times N_2 = 64 \times 64$.

Comparing the Reynolds numbers, we notice at Re = 1 the existence of two symmetry planes at $x_1 = 1$ and $x_2 = 0.5$ for both flow directions. At Re = 100, there is only one plane of symmetry: $x_2 = 0.5$ for flow along the x_1-axis, and $x_1 = 1$ for flow along the x_2-axis. The flow patterns, however, are much more intricate at Re = 100 than they are at Re = 1. For flow along the x_1-axis we notice several recirculation zones near bends in the flow field, as the fluid has separated near the sharp edges of the obstructing solid bodies. These recirculation zones constrict the main path of flow and locally increase the fluid velocity. As a consequence higher fluid resistance is experienced. For the flow along the x_2-axis, pockets of recirculating fluid develop inside the cavities between adjacent solid bodies and the bulk fluid motion resembles plane-

Table 1
Effect of Reynolds number and grid resolution on the macroscopic pressure gradient for the inline arrangement of square rods (porosity $\phi = 0.75$). The relative error in % (relative to Ref. [21]) is denoted by δ in the third column.

Re	$-\frac{\partial \langle p \rangle^f}{\partial x_1}$	$\delta - \frac{\partial \langle p \rangle^f}{\partial x_1}$	$N_1 \times N_2 \times N_3$
10	**7.82**	0%	$181 \times 181 \times 1$ (Ref. [21])
	6.65	−15%	$32 \times 32 \times 4$
	7.16	−8.4%	$64 \times 64 \times 4$
	7.45	−4.7%	$128 \times 128 \times 4$
100	**0.835**	0%	$181 \times 181 \times 1$ (Ref. [21])
	0.711	−15%	$32 \times 32 \times 4$
	0.768	−8.0%	$64 \times 64 \times 4$
	0.800	−4.2%	$128 \times 128 \times 4$
600	**0.154**	0%	$181 \times 181 \times 1$ (Ref. [21])
	0.124	−20%	$32 \times 32 \times 4$
	0.135	−12%	$64 \times 64 \times 4$
	0.143	−7.1%	$128 \times 128 \times 4$
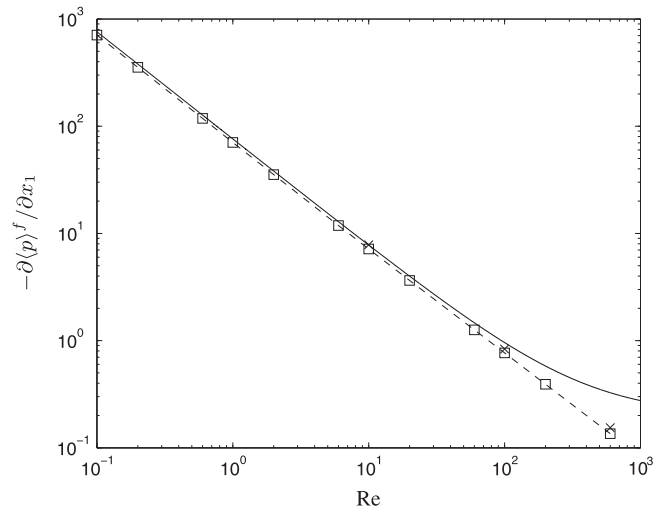
Fig. 7. Macroscopic pressure gradient for the inline arrangement of square rods at a range of Reynolds numbers and at a porosity $\phi = 0.75$. The solid line represents the Forchheimer extended Darcy's law with parameters computed in Refs. [21,22]. The dashed line [with ($\square$)-markers] represents our computed results at a resolution of $N_1 \times N_2 = 64 \times 64$. The ($\times$)-markers indicate values for the macroscopic pressure gradient at Re $\in \{10, 100, 600\}$, as found in Ref. [21].
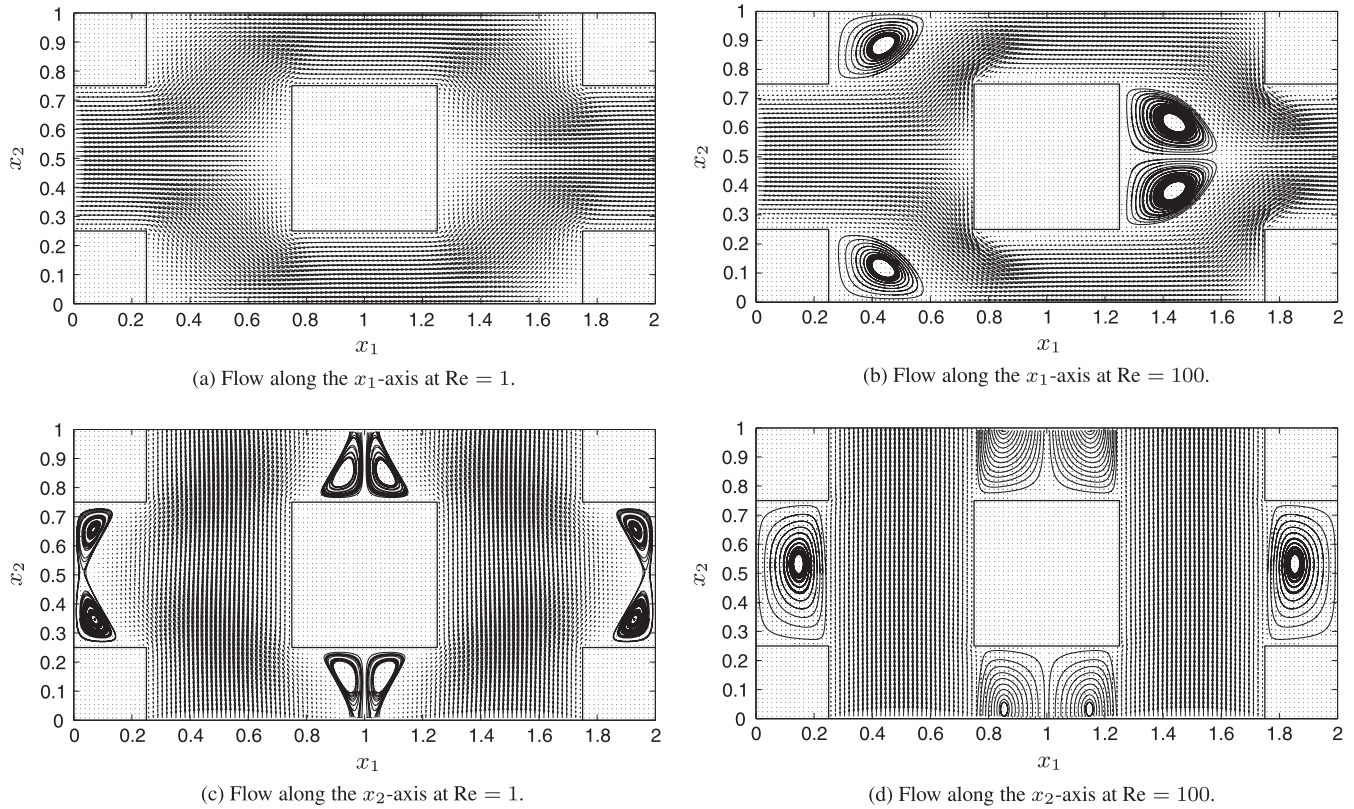
Poiseuille flow; with its characteristic parabolic velocity profile. In general, the flow behavior along the x_2-axis resembles the behavior seen for the inline arrangement (see Fig. 6).

4. Apparent permeability of a staggered arrangement of square rods

In this section the apparent permeability is computed for the staggered arrangement of square rods at various Reynolds numbers (Section 4.2) and porosities (Section 4.3). We include the directional dependency (anisotropy) of the apparent permeability by computing its values along the three coordinate axes. To be able to investigate this anisotropy we first require the definition of the scalar "directional permeability" (Section 4.1).

4.1. Extended Darcy's law and directional permeability

In this subsection we show how the directional permeability can be computed from the microtransport data. Its computation requires a few intermediate steps, these are discussed in detail below.

(a) Flow along the x_1-axis at Re = 1.

(b) Flow along the x_1-axis at Re = 100.

(c) Flow along the x_2-axis at Re = 1.

(d) Flow along the x_2-axis at Re = 100.

Fig. 8. Velocity vector field in the (x_1, x_2)-plane at two Reynolds numbers Re $\in \{1, 100\}$ for the staggered arrangement of square rods. The streamlines help visualize the dynamics in recirculation zones. The porosity ϕ = 0.75 and the grid resolution in the (x_1, x_2)-plane is $N_1 \times N_2$ = 128 × 64.

A common approach to modeling predominantly viscous flow through a homogeneous porous medium is to assume the macro-scale (or coarse scale) system obeys Darcy's law [6,7]. Darcy's law is a proportionality relation between the average fluid velocity $\langle \mathbf{u} \rangle$ and the macroscopic pressure gradient $\nabla \langle p \rangle^f$. The constant of proportionality, for isotropic porous media, contains the scalar permeability K. For anisotropic media, a generalized form of Darcy's law can be proposed [6,7]:

$$\langle \mathbf{u} \rangle = -\text{Re } \mathbf{K} \nabla \langle p \rangle^f. \tag{35}$$

Here we have expressed it in dimensionless form where Re the Reynolds number and $\mathbf{K}$ is now the permeability tensor. In an anisotropic porous medium the vectors $\langle \mathbf{u} \rangle$ and $\nabla \langle p \rangle^f$ are non-colinear except when they are in the direction of one of the principal axes [6,7]. The permeability can generally be interpreted as the inverse of a "resistance" parameter, influencing the flow of fluid inside a porous medium. A large value of the permeability, for a given driving force $\nabla \langle p \rangle^f$, results in a large throughput of fluid. The Darcy's law permeability tensor $\mathbf{K}$ is a material property dependent only on the geometrical structure of the porous medium [6,7]. Also, it has been shown [6,7,24] that for all porous media the permeability tensor is symmetric and positive definite.

The validity of Darcy's law starts to break down as inertial forces become more important [6,7]. This effect is clearly visible at the microscale, where the non-linear nature of the fluid produces regions of vortical motion [5] which can drastically affect the hydrodynamic drag. The intensity, size and stability of these vortices depend not only on the geometrical structure of the porous medium but also on the Reynolds number. Consequently, for inertial flows the linear relation of Eq. (35) is extended into the *non-linear laminar regime* [7] using the Forchheimer extended Darcy's law [14]:

$$\langle \mathbf{u} \rangle = -\text{Re } \mathbf{K} \nabla \langle p \rangle^f - \mathbf{F} \langle \mathbf{u} \rangle, \tag{36}$$

with $\mathbf{F}$ the Forchheimer correction tensor. In general, the Forchheimer tensor $\mathbf{F}$ is dependent on the Reynolds number and on the geometrical structure of the porous medium. Therefore, a universally valid expression for $\mathbf{F}$ does not exist. Various numerical studies have uncovered geometry-specific relations for the permeability and Forchheimer tensor as functions of the Reynolds number and flow angle, e.g., the work on inline-arrangements of square rods in Refs. [21,22]. It should be pointed out that both Eqs. (35) and (36) are subject to certain assumptions in their derivation (from the volume-averaged Navier–Stokes equations [14,30]) and therefore describe macroscopic flow behavior with a certain accuracy level only in a range of Reynolds numbers. This range of acceptable accuracy is strongly dependent on the geometry of the porous medium being considered. By a proper parameterization of the tensors $\mathbf{K}$ and $\mathbf{F}$ this range may be enlarged. Finding suitable values for the components of these tensors is of great importance to engineering transport models.

We will model macroscopic flow behavior according to Ref. [5], where the concept of an *apparent permeability* was introduced; that is, a permeability not only dependent on the pore geometry but also on the Reynolds number. We derive the apparent permeability by simply rewriting Eq. (36):

$$\langle \mathbf{u} \rangle = -\text{Re } (\mathbf{I} + \mathbf{F})^{-1} \mathbf{K} \nabla \langle p \rangle^f = -\text{Re } \mathbf{k} \nabla \langle p \rangle^f, \tag{37}$$

which introduces $\mathbf{k} \equiv (\mathbf{I} + \mathbf{F})^{-1} \mathbf{K}$ as the apparent permeability tensor. Eq. (37) maintains the simple Darcy-type formulation for macroscale transport [see Eq. (35)] but with an increased range of applicability, as the apparent permeability $\mathbf{k}$ is now Reynolds number dependent and provides corrections in the inertial regime. The formulation of Eq. (37) allows for a single phenomenological parameter to quantify the permeable nature of a porous medium.

Given the value of **k** for a very low Reynolds numbers (i.e., highly viscous flow) the Darcy's law permeability tensor $\mathbf{K} \approx \mathbf{k}$ and $\mathbf{F} \approx 0$. The value of **F** is relevant at higher Reynolds numbers and is computed by solving for it in the relation: $\mathbf{k}\mathbf{K}^{-1} = (\mathbf{I} + \mathbf{F})^{-1}$.

In general, the nine components k_{ij} of the apparent permeability tensor **k** can be computed by simulating the microscale velocity and pressure fields within a REV of a porous medium. When the Reynolds number is sufficiently low the linearity between the average fluid velocity and the macroscopic pressure gradient (i.e., Darcy's law) allows for the components of **k** to be approximated as constants. As $\mathbf{k} \approx \mathbf{K}$ and symmetric, the now *six* components can be computed by simulating the flow in six independent directions. More specifically, we must solve six independent flow problems involving a macroscopically one-dimensional, steady flow. Every flow direction produces a so-called "directional" apparent permeability [6,7] (or just *directional permeability* for short) that can be coupled back to the tensor components k_{ij}. The directional permeability is a specific *scalar* form of the apparent permeability that characterizes flow resistance along a prescribed direction **n** of the macroscopic flow. Its definition follows from a Darcy-type relation where the average velocity and macroscopic pressure gradient are aligned along a direction **n** [6,7,45,46]. It is computed as follows: set a macroscopically uniform flow $\langle\mathbf{u}\rangle = \mathbf{n}|\langle\mathbf{u}\rangle|$ (of strength $|\langle\mathbf{u}\rangle|$ and direction **n**) and take the component of the macroscopic pressure gradient in the direction of flow, $\mathbf{n} \cdot \nabla\langle p\rangle^f$, the directional permeability then follows from

$$|\langle\mathbf{u}\rangle| = -\text{Re } k_{\mathbf{n}}(\mathbf{n} \cdot \nabla\langle p\rangle^f), \tag{38}$$

such that

$$k_{\mathbf{n}} = -\frac{|\langle\mathbf{u}\rangle|}{\text{Re } (\mathbf{n} \cdot \nabla\langle p\rangle^f)}. \tag{39}$$

The relationship between the directional permeability $k_{\mathbf{n}}$ and the components k_{ij} of the apparent permeability tensor **k** can easily be derived by noticing that:

$$\mathbf{n} \cdot \nabla\langle p\rangle^f = \mathbf{n} \cdot \left(-\frac{1}{\text{Re}}\mathbf{k}^{-1}\langle\mathbf{u}\rangle\right) = -\frac{1}{\text{Re}}\mathbf{n} \cdot (\mathbf{k}^{-1}\mathbf{n})|\langle\mathbf{u}\rangle|, \tag{40}$$

where we made use of Eq. (37). By comparing Eqs. (38) and (40) gives [6,7,45,46]:

$$k_{\mathbf{n}} = \frac{1}{\mathbf{n} \cdot (\mathbf{k}^{-1}\mathbf{n})}. \tag{41}$$

We can further simplify **k** at low Reynolds numbers if the porous medium is orthotropic (i.e., having three mutually orthogonal principal axes [6,7]) such that **k** can assume a diagonal form. This then reduces the unknown tensor components k_{ij} from six to *three*.

At higher Reynolds numbers, where non-linear flow effects are present, the tensor **k** need not be symmetric nor constant. It must account for potentially strong changes in dynamical flow patterns. For steady flow, the nine components k_{ij} follow in this most general setting from nine independent flow simulations. It is common practice to parameterize the components in terms of the Reynolds number. However, for strongly non-linear (e.g., turbulent) flows this parameterization breaks down as the flow becomes time-dependent. Also, with increasing Reynolds number the macroscopic properties of the flow along an arbitrary direction do not correlate with the macroscopic properties along different flow directions.

For the staggered arrangement of square rods we will treat its principal axes as orthogonal and that they coincide with the coordinate axes [see Fig. 5b]. We can then assume that for low to moderate Reynolds numbers (i.e., for weakly-non-linear flow) the dominant flow dynamics are along the three principal axes. We will compute the three diagonal components in the tensor **k** and

parameterize them in terms of the Reynolds number. The macroscopic flow behavior in an arbitrary direction is now expressed as a linear combination of the flow behavior along each of the three coordinate axes.

In the following subsections predictions for the directional permeability will be made using Eq. (39), where we specify a macroscopically uniform flow (through a constant flow rate **Q**) and compute the resulting macroscopic pressure gradient. We will study the effects of a varying Reynolds number and porosity on the directional permeability. Varying the Reynolds number will illustrate the effects associated with the transition from the purely viscous to the inertial regime. The changes in porosity will illustrate effects arising from a changing inner structure of the porous medium. We consider the direction of flow along each of the three coordinate axes. All numerical predictions are performed on a range of grid resolutions to investigate the grid sensitivity of the IB method.

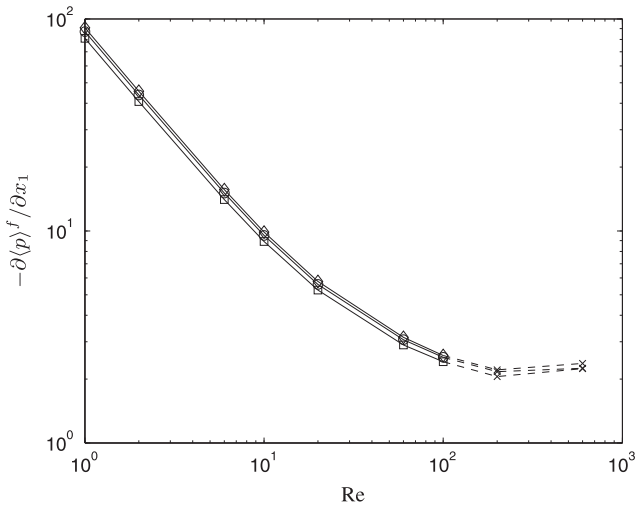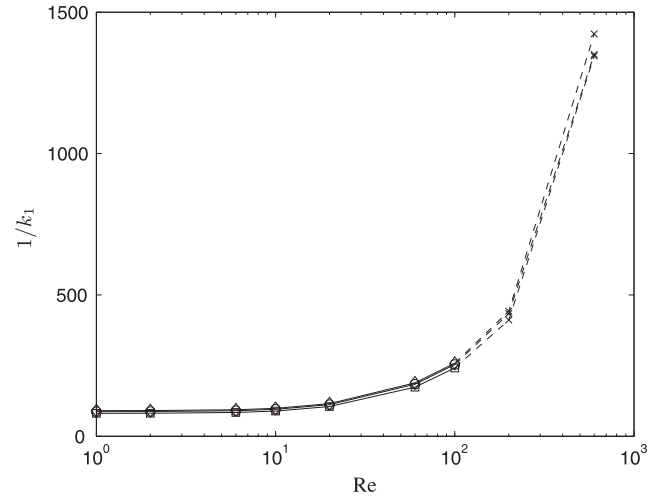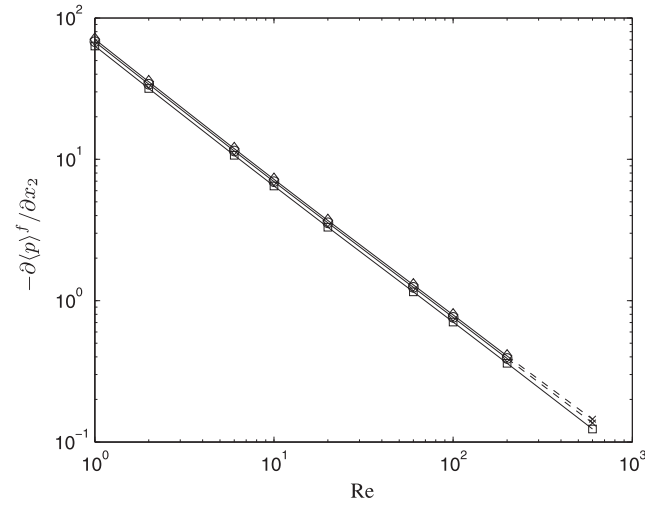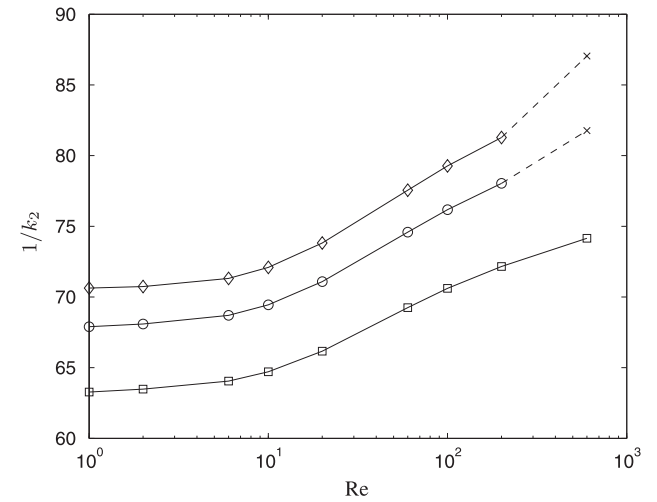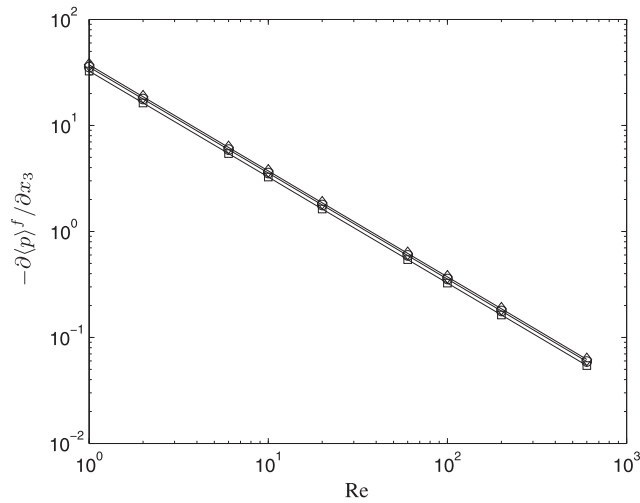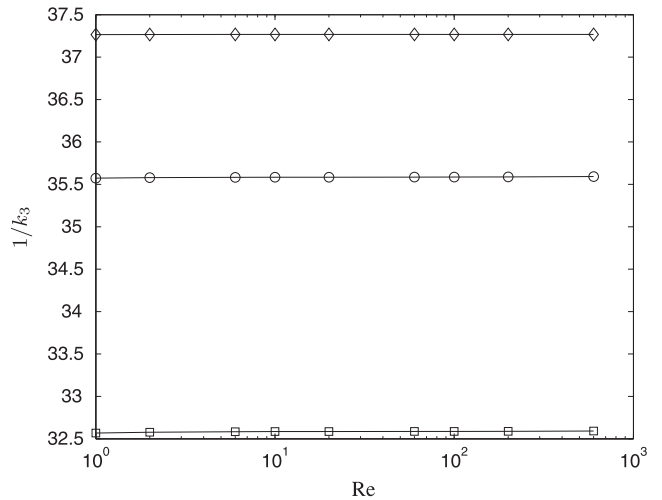### 4.2. Effect of Reynolds number on the directional permeability

The effect of the Reynolds number on the directional permeability will be computed for the staggered arrangement of square rods, as defined in Fig. 5b. The Reynolds number, a ratio of inertial forces to viscous forces, quantifies the relative importance of these forces for the transport of momentum. Increasing the Reynolds number changes the flow pattern from a smoothly varying flow field to a more dynamic flow field, with separation zones and other forms of vortical structures. This increase will have an obvious effect on the directional permeability. To quantify the behavior of the directional permeability, we need to first compute the macroscopic pressure gradient and examine its change with an increase in the Reynolds number. Through Eq. (39) we can then compute the directional permeability. Also, having knowledge of the macroscopic pressure gradient as a function of the Reynolds number enables us to verify whether these results actually satisfy a Darcy-type relation. In that case, the macroscopic pressure gradient correlates with the averaged velocity according to a functional relation similar to Eq. (38).

We will consider the flow of fluid along the three coordinate axes $\{x_1, x_2, x_3\}$ and a porosity $\phi = 0.75$. We denote the directional permeability along the axes $\{x_1, x_2, x_3\}$ by $\{k_1, k_2, k_3\}$, respectively. In Fig. 9 we plot values of the macroscopic pressure gradient $-\partial\langle p\rangle^f/\partial x_i$ and the directional permeability $1/k_i$ ($i \in \{1, 2, 3\}$) for a range of Reynolds numbers. The macroscopic pressure gradient is computed according to Eq. (30f). We incorporate results on three grid resolutions $N_1 \times N_2 \times N_3$, including: $64 \times 32 \times 4$, $128 \times 64 \times 4$, and $256 \times 128 \times 4$. We will ignore subsequent grid refinements along the x_3-axis as numerical experiments have demonstrated $-\partial\langle p\rangle^f/\partial x_i$ to be independent of N_3. The flow field is actually fully independent of x_3. Therefore, a minimum grid resolution of $N_3 = 4$ is chosen along the x_3-axis. Fig. 9a, c and e all indicate monotonically decreasing values for the pressure gradient $-\partial\langle p\rangle^f/\partial x_i$ with increasing Reynolds number (at least for the steady cases). Estimates for a functional relation between the macroscopic pressure gradient and the Reynolds number can be made by assuming a power law behavior of the kind:

$$-\frac{\partial\langle p\rangle^f}{\partial x_i} \approx a_i \text{ Re}^{-b_i} + c_i, \tag{42}$$

with coefficients $\{a_i, b_i, c_i\} \geqslant 0$ and $i \in \{1, 2, 3\}$. For the case that $b_i = 1$ and $c_i = 0$ the original Darcy's law is recovered, where $a_i = |\langle u_i\rangle|/k_i$ and k_i is the constant Darcy's law permeability. The coefficient c_i can be made Reynolds number dependent in order to describe a wider class of functional relations between the macroscopic pressure gradient and the Reynolds number. Using

(a) Macroscopic pressure gradient along the x_1-axis.

(b) Directional permeability along the x_1-axis.

(c) Macroscopic pressure gradient along the x_2-axis.

(d) Directional permeability along the x_2-axis.

(e) Macroscopic pressure gradient along the x_3-axis.

(f) Directional permeability along the x_3-axis.

Fig. 9. Macroscopic pressure gradient and directional permeability at various values of the Reynolds number and the grid resolution for the staggered arrangement of square rods. The grid resolution is indicated by the following markers: ($\square$)-markers, $64 \times 32 \times 4$; ($\bigcirc$)-markers, $128 \times 64 \times 4$; and ($\diamond$)-markers, $256 \times 128 \times 4$. The porosity $\phi = 0.75$. Values indicated by the ($\times$)-marker are unsteady, and a time-averaged approximation is taken.

Fig. 9, we can estimate values for the coefficients $\{b_i, c_i\}$ by simply observing the global behavior of the macroscopic pressure gradient and the directional permeability. These estimates will help identify in which direction and for which Reynolds numbers the Darcy's law holds, and for which cases corrections are required.

- For flow along the x_1-axis: $b_1 \leqslant 1$ and $c_1 > 0$; as $-\partial\langle p\rangle^f/\partial x_1$ decreases linearly (with constant slope) and then flattens out at higher Reynolds numbers (up to Re $\approx$ 200), and $1/k_1$ increases monotonically.
- For flow along the x_2-axis: $b_2 \leqslant 1$ and $0 < c_2 \ll 1$; as $-\partial\langle p\rangle^f/\partial x_2$ decreases linearly and $1/k_2$ increases in a non-linear fashion.
- For flow along the x_3-axis: $b_3 = 1$ and $c_3 = 0$; as $-\partial\langle p\rangle^f/\partial x_3$ decreases linearly and $1/k_3$ is constant.

From these observations it is evident that flow along the $\{x_1, x_2\}$-axes (for the considered Reynolds numbers) exhibit a non-Darcy type flow description, where the macroscopic pressure gradient is not directly proportional to the average velocity. Inertial corrections to the Darcy's law are required for these directions. In terms of the Forchheimer extended Darcy's law, corrections can be incorporated through a Reynolds number dependent Forchheimer tensor. To demonstrate this, we consider the "directional" form of the Forchheimer extended Darcy's law by expanding $k_\mathbf{n}$ in Eq. (38) in terms of the directional Darcy's law permeability $K_\mathbf{n}$ and the directional Forchheimer coefficient $F_\mathbf{n}$. Along the three coordinate axes, this yields for $i \in \{1, 2, 3\}$:

$$-\frac{\partial\langle p\rangle^f}{\partial x_i} = \frac{|\langle u_i\rangle|}{K_i}\,\mathrm{Re}^{-1} + \frac{|\langle u_i\rangle|}{K_i}\,\mathrm{Re}^{-1}F_i = \frac{\frac{1}{K_i} + \frac{1}{K_i}F_i}{\mathrm{Re}}, \quad (43)$$

where $|\langle u_i\rangle| = 1$ for all $i \in \{1, 2, 3\}$ in the simulations. By rewriting expression (42)

$$a_i\,\mathrm{Re}^{-b_i} + c_i = a_i\,\mathrm{Re}^{-1} + \left(a_i\,\mathrm{Re}^{-b_i} + c_i\right) - a_i\,\mathrm{Re}^{-1}$$

$$= \frac{a_i + a_i\left(-1 + \mathrm{Re}^{1-b_i} + \frac{c_i}{a_i}\,\mathrm{Re}\right)}{\mathrm{Re}}, \quad (44)$$

and comparing Eqs. (43) and (44) yields for the directional coefficients:

$$K_i = \frac{1}{a_i}, \quad (45a)$$

$$F_i = -1 + \mathrm{Re}^{1-b_i} + \frac{c_i}{a_i}\,\mathrm{Re}. \quad (45b)$$

The flattening of the curve in Fig. 9a can be contributed to the development of recirculation zones within the domain that constrict the primary path of fluid flow. These recirculation zones are clearly visible in Fig. 8b. The behavior of the flow along the x_2-axis is similar to that found for the inline arrangement, as can be seen in Figs. 6 and 8c and d.

Estimates for the directional permeability follow directly from Eq. (39) and expression (42), where for $i \in \{1, 2, 3\}$:

$$\frac{1}{k_i} \approx a_i\,\mathrm{Re}^{1-b_i} + c_i\,\mathrm{Re}. \quad (46)$$

All values of k_i (apart from k_3 which is constant) decrease with an increasing Reynolds number. The decrease in the directional permeability (or increase in $1/k_i$) with increasing fluid inertia is directly related to the local flow field, with its vortical structures and flow constrictions (see Fig. 8). The observed uniformity of k_3 with respect to the Reynolds number is consistent with known behavior of laminar flows in domains of constant cross section. To motivate this, consider laminar fully-developed flow in a channel of constant cross section. In channel flow the friction force experienced by the fluid, expressed using the *friction factor* $\mathfrak{f}$ [12, Chapter 6], decreases

as a function of the Reynolds number (for a constant flow rate), such that $\mathfrak{f} = $ constant/Re. As the global pressure drop is proportional to the friction factor [12], $\nabla P \propto \mathfrak{f}$, using Eq. (39) it follows that the permeability k is independent of Re for a constant flow rate (i.e., constant $\langle u\rangle$). As for the staggered arrangement, the cross section of the flow domain does not change along the x_3-axis, we therefore expect that $\log(-\partial\langle p\rangle^f/\partial x_3)$ versus $\log(\mathrm{Re})$ decreases with slope 1 [see Fig. 9e], and that $1/k_3$ is independent of Re (given that $\langle u_3\rangle$ is constant) [see Fig. 9f].

A comparison of the simulation results for various grid resolutions reveals a weak dependence of the coefficients $\{b_i, c_i\}$ on spatial refinements (see Fig. 9 and Table 2). For example, in Fig. 9, we notice that the slope of the pressure gradient curve (or the trend of the directional permeability curve) is captured very well even at a modest grid resolution of $64 \times 32 \times 4$; albeit a low resolution overpredicts the directional permeability k_i for all $i \in \{1, 2, 3\}$. The coefficient a_i, however, is more sensitive to the grid resolution. Table 3 contains values of the directional permeability $1/k_i$ ($i \in \{1, 2, 3\}$) at three Reynolds numbers and at three grid resolutions. We observe that the values of $1/k_i$ are not yet fully converged at the selected resolutions. More accurate results are expected with an improved IB method, which is the subject of ongoing research. Also, the slight variation of $1/k_3$ with the Reynolds number is contributed to the flow field being under-resolved at the two lowest grid resolutions. Nevertheless, the main consequences for the permeability arising from differences in the physical domain "seen" when flowing along the three coordinate axes can be reliably captured with the current first-order accurate method.

Fig. 9 also indicates values of the Reynolds number where the flow field becomes unsteady [indicated by the ($\times$)-markers]. For these cases a time-averaging of the macroscopic pressure gradient has been performed. Along the x_2-axis the onset of unsteady flow appears earlier at higher resolutions.

Table 2
Estimates for the coefficients $\{a_i, b_i, c_i\}$ in expressions (42) and (46) at three grid resolutions for the staggered arrangement of square rods ($i \in \{1, 2, 3\}$). The porosity ϕ = 0.75.

Flow axis	$N_1 \times N_2 \times N_3$	a_i	b_i	c_i
x_1-Axis	$64 \times 32 \times 4$	81	0.96	1.4
	$128 \times 64 \times 4$	87	0.96	1.5
	$256 \times 128 \times 4$	91	0.96	1.6
x_2-Axis	$64 \times 32 \times 4$	63	0.99	0.01
	$128 \times 64 \times 4$	68	0.99	0.03
	$256 \times 128 \times 4$	71	0.99	0.03
x_3-Axis	$64 \times 32 \times 4$	33	1	0
	$128 \times 64 \times 4$	36	1	0
	$256 \times 128 \times 4$	37	1	0

Table 3
Computed values for the directional permeability $1/k_i$ ($i \in \{1, 2, 3\}$) at three Reynolds numbers and at three grid resolutions for the staggered arrangement of square rods. The porosity ϕ = 0.75.

Flow axis	$N_1 \times N_2 \times N_3$	Re = 1	Re = 10	Re = 100
x_1-Axis	$64 \times 32 \times 4$	81.03	89.10	241.5
	$128 \times 64 \times 4$	87.16	95.30	253.4
	$256 \times 128 \times 4$	90.84	98.78	258.5
x_2-Axis	$64 \times 32 \times 4$	63.28	64.71	70.61
	$128 \times 64 \times 4$	67.90	69.45	76.18
	$256 \times 128 \times 4$	70.63	72.09	79.27
x_3-Axis	$64 \times 32 \times 4$	32.57	32.59	32.59
	$128 \times 64 \times 4$	35.57	35.58	35.59
	$256 \times 128 \times 4$	37.27	37.27	37.27
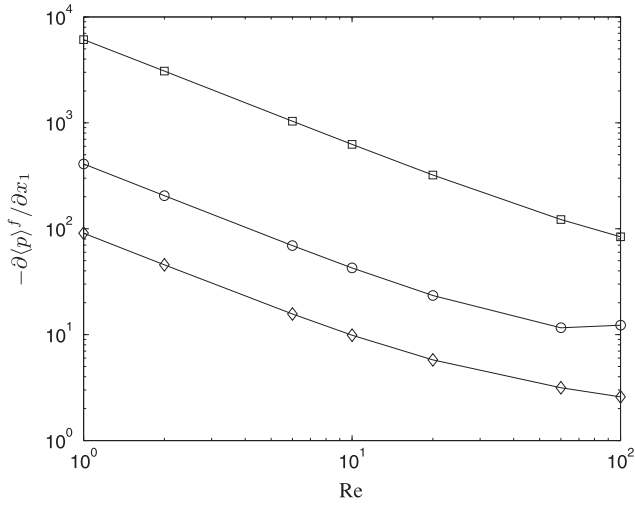
(a) Macroscopic pressure gradient along the x_1-axis.
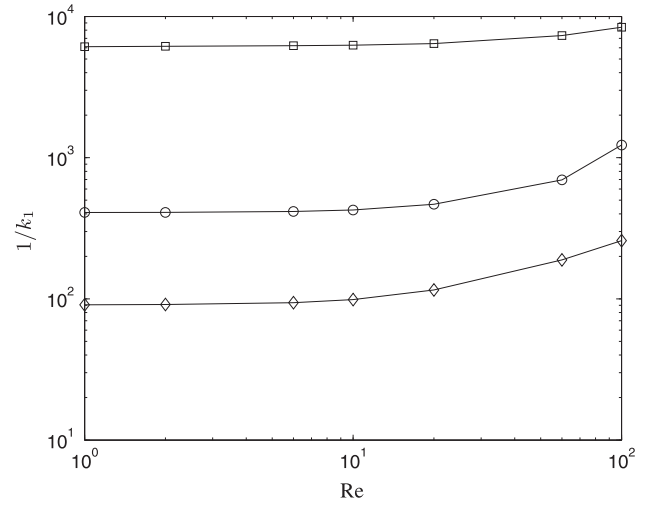
(b) Directional permeability along the x_1-axis.
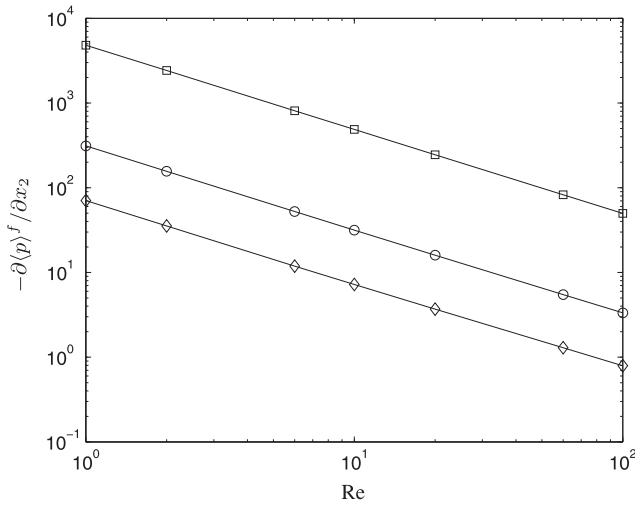
(c) Macroscopic pressure gradient along the x_2-axis.
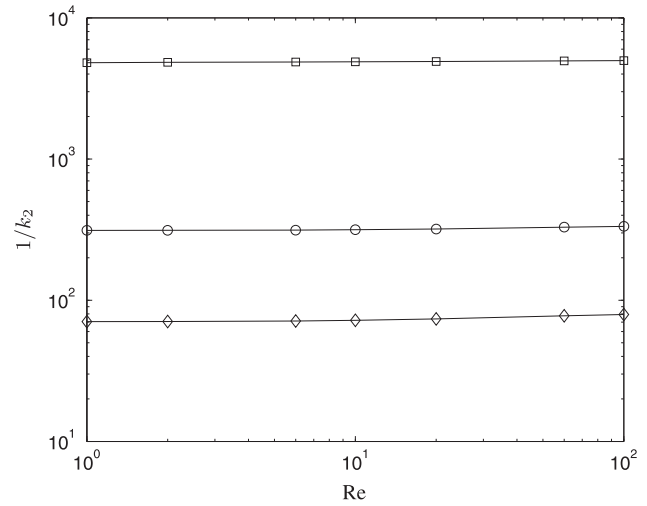
(d) Directional permeability along the x_2-axis.
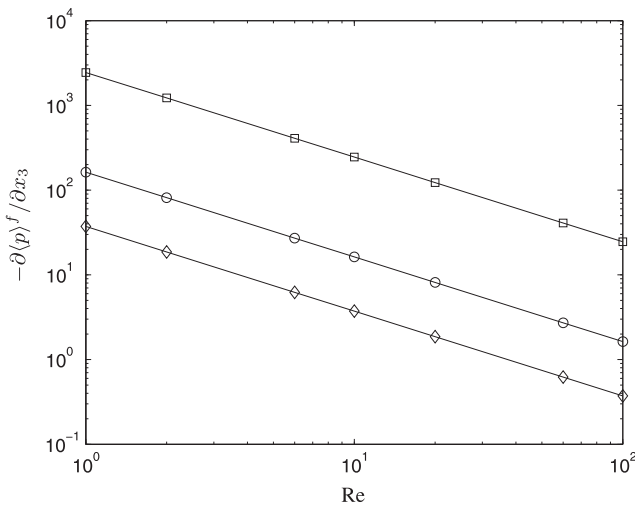
(e) Macroscopic pressure gradient along the x_3-axis.
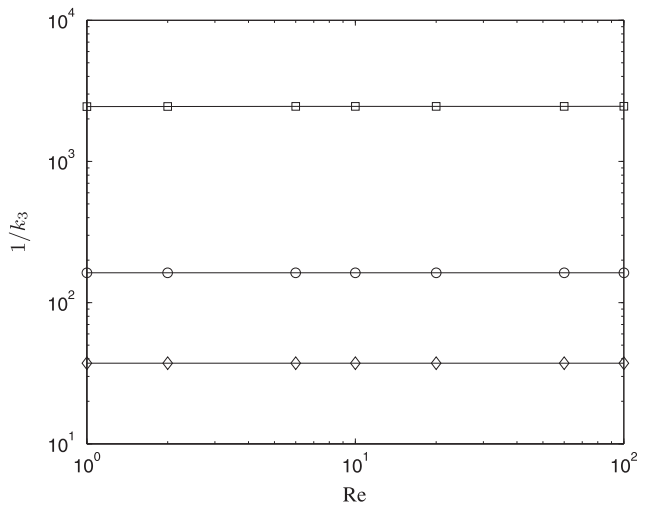
(f) Directional permeability along the x_3-axis.

Fig. 10. Macroscopic pressure gradient and directional permeability at various values of the Reynolds number and the porosity for the staggered arrangement of square rods. The porosity ϕ is indicated by the following markers: ($\square$)-markers, $\phi = 0.2344$; ($\bigcirc$)-markers, $\phi = 0.5273$; and ($\diamond$)-markers, $\phi = 0.75$. The grid resolution is set to $N_1 \times N_2 \times N_3 = 256 \times 128 \times 4$.

4.3. Effect of porosity on the directional permeability

The porosity ϕ of a porous medium is a measure for the packing-density of its solid material. It is defined as the ratio of the fluid volume within $\mathcal{V}$ to the total volume of $\mathcal{V}$, where $\mathcal{V}$ is a REV of the porous medium [see Eq. (5)]. The lower the porosity, the higher the packing-density, and the narrower the interstitial fluid channels become. By considering a variable porosity we can investigate the effect of "flow constriction" on the behavior of the directional permeability. For the staggered arrangement of square rods the porosity is defined as $\phi = 1 - (D/H)^2$. We will consider the variation of ϕ under a constant H, i.e., we will vary the dimension D of the solid bodies. We also consider a range of Reynolds numbers for which the flow remains steady, therefore setting an upperbound for the Reynolds number of Re $\leqslant$ 100. The effect of porosity on the directional permeability is investigated along the three coordinate axes $\{x_1, x_2, x_3\}$.

Intuitively, we can imagine that a decrease in the porosity will result in a decrease in the directional permeability (under identical flow rates). This decrease is directly related to the increased resistance experienced by the fluid flowing through the narrowing channels. The total resistance (e.g., due to wall friction and recirculation zones) is also related to the inertia of the flow, and will therefore further increase with increasing Reynolds number. Using the simulation results we can also address the question whether a macrotransport relation similar to expression (42) holds for the macroscopic pressure gradient for different porosity values. We will approach this question by studying the flow through the staggered arrangement of squares at two new porosities ϕ, which will represent a solidity of approximately 50% and 75% of the total volume $\mathcal{V}$. To achieve these porosities we set $D = \sqrt{1 - \phi}H$. Note, however, that the actual values of ϕ depend on the spatial resolution of the computational grid. This is because the solid bodies are represented by a collection of grid cells. Therefore, in terms of the number of grid cells across its length, $D = \sqrt{1 - \phi}N_2\Delta x_2$; where N_2 is the grid resolution along the x_2-axis and Δx_2 is the grid spacing along the x_2-axis.

In Fig. 10 we plot computed values for the macroscopic pressure gradient $-\partial\langle p\rangle^f/\partial x_i$ and the directional permeability $1/k_i$ ($i \in \{1, 2, 3\}$) at a range of Reynolds numbers. The two new values for the porosity $\phi \in \{0.2344, 0.5273\}$ are plotted along with the value of $\phi = 0.75$ from the previous section. The grid resolution is set to $N_1 \times N_2 \times N_3 = 256 \times 128 \times 4$. At this resolution the length D of the solid square occupies $N_D = \sqrt{1 - \phi}N_2 = \{112, 88, 64\}$ grid cells for $\phi = \{0.2344, 0.5273, 0.75\}$, respectively. It is evident from Fig. 10 that the macroscopic flow behavior at $\phi \in \{0.2344, 0.5273\}$ is similar to the behavior at $\phi = 0.75$; with a difference only in the "amplitude" of the curves. This indicates that for the considered range of porosities, the power law behavior as expressed in (42) and (46) remains a valid approximation for the macroscopic pressure gradient and the directional permeability,

respectively. The Forchheimer extended Darcy's law appears suitable for macrotransport modeling in the range studied.

For detailed reference we list values for the directional permeability at three Reynolds numbers and for the three porosities in Table 4. We observe that a decrease in the porosity results in a strong increase in the flow resistance. The strong non-linear increase has important consequences for the modeling of transport phenomena in realistic porous media, as natural variations in the local porosity are to be expected.

5. Conclusions

A volume-averaged description of the transport of fluid in porous media requires the introduction of macroscopic transport parameters to represent sub-filter scale effects. The parameter of interest in this work has been the apparent permeability, a combination of the Darcy's law permeability tensor and the Forchheimer tensor. We have proposed a numerical simulation strategy for computing the apparent permeability of a model porous medium composed of a staggered arrangement of square rods. The numerical approach was used to investigate the effects of the Reynolds number, porosity and flow direction on the apparent permeability.

The proposed simulation strategy was based on solving the incompressible Navier–Stokes equations for fluid transport in a representative elementary volume of the porous medium. We utilized a volume-penalizing immersed boundary method to approximate the momentum interaction between a solid body and the fluid. The algorithmic implementation of the method required a Cartesian grid representation of the computational domain, thereby eliminating the need for the generation of a body-conforming grid. Microscopic velocity and pressure fields were processed using the Forchheimer extended Darcy's law to compute the apparent permeability.

We presented a validation of the method using a model porous medium composed of an inline arrangement of square rods. The macroscopic pressure gradient has been compared with available results from literature for various Reynolds numbers. A convergence rate indicative of a first-order spatial discretization was observed. As a consequence, high grid resolution was required to obtain quantitatively accurate results. On the finest grid resolution, a relative error of approximately 7% was measured at the highest Reynolds number Re = 600. At lower Reynolds numbers, the relative error decreased to about 4–5%. However, at coarse resolutions the method did manage to capture accurately the trend line of the macroscopic pressure gradient for Reynolds numbers up to Re = 600. The strength of the proposed immersed boundary method is its gridding-free strategy and its ability to use fast numerical solvers that benefit from the Cartesian grid representation.

A systematic parameter study has been performed for a staggered arrangement of square rods to help understand the relation between the microscale fluid motion and the apparent permeability of the model porous medium. We considered the effect of changing the Reynolds number by performing simulations over the range $1 \leqslant$ Re $\leqslant 600$. We also considered the effect of a change in porosity, where three values were selected ranging from 25% fluid volume fraction to 75%. The anisotropy of the apparent permeability was investigated by considering flow along the three coordinate axes. From the microscale simulations we were able to confirm that the Forchheimer extended Darcy's law is a valid model for predicting macroscopically steady and uniform flow in the staggered arrangement. On this basis an accurate engineering model can be formulated that may be specifically calibrated using simulation results. This illustrates the strength of computational modeling, giving access to material and flow parameters that are otherwise difficult to obtain and interpret experimentally.

Table 4
Computed values for the directional permeability $1/k_i$ ($i \in \{1, 2, 3\}$) at three Reynolds numbers and at three porosities for the staggered arrangement of square rods. The grid resolution is $N_1 \times N_2 \times N_3 = 256 \times 128 \times 4$.

Flow axis	ϕ	Re = 1	Re = 10	Re = 100
x_1-Axis	0.2344	6104	6257	8383
	0.5273	409.0	426.3	1228
	0.75	90.84	98.78	258.5
x_2-Axis	0.2344	4814	4880	4979
	0.5273	312.4	315.8	333.5
	0.75	70.63	72.09	79.27
x_3-Axis	0.2344	2445	2455	2456
	0.5273	162.8	162.8	162.8
	0.75	37.27	37.27	37.27

Topics of ongoing research include: improvements in accuracy of the immersed boundary method, and an extension to incorporate heat and mass transfer. These topics will pave the way for the development of a reliable simulation tool capable of realistic geometries and complex physical processes.

Acknowledgments

References

[1] Oliveira AAM, Kaviany M. Prog Energy Combust Sci 2001;27:523.
[2] Tien C, Payatakes AC. AIChE J 1979;25:737.
[3] Nordlund M, Lundström TS. J Compos Mater 2005;39:929.
[4] Whitaker S. The method of volume averaging. Dordrecht: Kluwer Academic Publishers; 1999.
[5] Edwards DA, Shapiro M, Bar-Yoseph P, Shapira M. Phys Fluids A 1990;2:45.
[6] Dullien FAL. Porous media: fluid transport and pore structure. New York: Academic Press, Inc.; 1979.
[7] Bear J. Dynamics of fluids in porous media. New York: Dover Publications, Inc.; 1988.
[8] Verstappen RWCP, Veldman AEP. J Comput Phys 2003;187:343.
[9] Mittal R, Iaccarino G. Annu Rev Fluid Mech 2005;37:239.
[10] Liu Q, Vasilyev OV. J Comput Phys 2007;227:946.
[11] Wildenschild D, Vaz CMP, Rivers ML, Rikard D, Christensen BSB. J Hydrol 2002;267:285.
[12] Bird RB, Stewart WE, Lightfoot EN. Transport phenomena. New York: John Wiley & Sons Inc.; 2002.
[13] Brenner H, Edwards DA. Macrotransport processes. Boston: Butterworth-Heinemann; 1993.
[14] Whitaker S. Transport Porous Media 1996;25:27.
[15] Zick AA, Homsy GM. J Fluid Mech 1982;115:13.
[16] Coulaud O, Morel P, Caltagirone JP. J Fluid Mech 1988;190:393.
[17] Koch DL, Ladd AJC. J Fluid Mech 1997;349:31.
[18] Hill RJ, Koch DL, Ladd AJC. J Fluid Mech 2001;448:213.
[19] Hill RJ, Koch DL, Ladd AJC. J Fluid Mech 2001;448:243.
[20] Sobera MP, Kleijn CR. Phys Rev E 2006;74:036301.
[21] Nakayama A, Kuwahara F, Umemoto T, Hayashi T. J Heat Transfer 2002;124:746.
[22] Nakayama A, Kuwahara F, Hayashi T. J Fluid Mech 2004;498:139.
[23] Mei CC, Auriault J-L. J Fluid Mech 1991;222:647.
[24] Hornung U, editor. Homogenization and porous media. New York: Springer-Verlag; 1997.
[25] Marie CM. Int J Eng Sci 1982;20:643.
[26] Gray WG. Chem Eng Sci 1975;30:229.
[27] Quintard M, Whitaker S. Transport Porous Media 1994;14:163.
[28] Quintard M, Whitaker S. Transport Porous Media 1994;14:179.
[29] Slattery JC. Momentum, energy, and mass transfer in continua. New York: McGraw-Hill; 1972.
[30] Whitaker S. Transport Porous Media 1986;1:3.
[31] Geurts BJ. Elements of direct and large-eddy simulation. Philadelphia: R.T. Edwards, Inc.; 2003.
[32] Lesieur M, Métais O. Annu Rev Fluid Mech 1996;28:45.
[33] Breugem W-P, Boersma BJ, Uittenbogaard RE. J Fluid Mech 2006;562:35.
[34] Ferziger JH, Perić M. Computational methods for fluid dynamics. Berlin: Springer-Verlag; 2002.
[35] Kuwahara F, Shirota M, Nakayama A. Int J Heat Mass Transfer 2001;44:1153.
[36] Wesseling P. Principles of computational fluid dynamics. Berlin: Springer-Verlag; 2001.
[37] Moin P, Kim J. J Fluid Mech 1982;118:341.
[38] Peskin CS. Annu Rev Fluid Mech 1982;14:235.
[39] Arquis E, Caltagirone JP. CR l'Academie Sci Ser II 1984;299:1.
[40] Angot P, Bruneau CH, Fabrie P. Numer Math 1999;81:497.
[41] Smolarkiewicz PK, Winter CL. J Comput Phys 2010;229:3121.
[42] Hirt CW, Nichols BD. J Comput Phys 1981;39:201.
[43] Batchelor GK. An introduction to fluid dynamics. Cambridge: Cambridge University Press; 2002.
[44] Mikhal J, Lopez Penha DJ, Stolz S, Geurts BJ. ASME Conf Proc 2010;2010:2453.
[45] Scheidegger AE. Pure Appl GeoPhys 1954;28:75.
[46] Scheidegger AE. Pure Appl GeoPhys 1956;33:111.